Oxidation State Dependence of the Geometry, Electronic Structure, and Magnetic Coupling in Mixed Oxo- and Carboxylato-Bridged Manganese Dimers

Christopher D. Delfs and Robert Stranger*

Department of Chemistry, The Australian National University, Canberra, ACT 0200, Australia

Received August 4, 2000

Approximate density functional theory has been used to investigate changes in the geometry and electronic structure of the mixed oxo- and carboxylato-bridged dimers $[Mn_2(\mu\text{-}O)_2(O_2CH)(NH_3)_6]^{n+}$ and $[Mn_2(\mu\text{-}O)(O_2CH)_2(NH_3)_6]^{n+}$ in the $Mn^{IV}Mn^{IV}$, $Mn^{III}Mn^{IV}$, and $Mn^{III}Mn^{III}$ oxidation states. The magnetic coupling in the dimer is profoundly affected by changes in both the bridging ligands and Mn oxidation state. In particular, change in the bridging structure has a dramatic effect on the nature of the Jahn−Teller distortion observed for the Mn^{III} centers in the III/III and III/IV dimers. The principal magnetic interactions in $[Mn_2(\mu\text{-}O)_2(O_2CH)(NH_3)_6]^{n+}$ involve the $J_{xz/xz}$ and $J_{yz/yz}$ pathways but due to the tilt of the Mn_2O_2 core, they are less efficient than in the planar di-μ-oxo structure and, consequently, the calculated exchange coupling constants are generally smaller. In both the III/III and III/IV dimers, the Mn^{III} centers are high-spin, and the Jahn−Teller effect gives rise to axially elongated Mn^{III} geometries with the distortion axis along the $Mn-O_c$ bonds. In the III/IV dimer, the tilt of the Mn_2O_2 core enhances the crossed exchange $J_{x^2-y^2/z^2}$ pathway relative to the planar di-μ-oxo counterpart, leading to significant delocalization of the odd electron. Since this delocalization pathway partially converts the Mn^{IV} ion into low-spin Mn^{III}, the magnetic exchange in the ground state can be considered to arise from two interacting spin ladders, one is the result of coupling between Mn^{IV} ($S = 3/2$) and high-spin Mn^{III} ($S = 2$), the other is the result of coupling between Mn^{IV} ($S = 3/2$) and low-spin Mn^{III} ($S = 1$). In $[Mn_2(\mu\text{-}O)(O_2CH)_2(NH_3)_6]^{n+}$, both the III/III dimer and the lowest energy structure for the III/IV dimer involve high-spin Mn^{III}, but the Jahn−Teller axis is now orientated along the Mn−oxo bond, giving rise to axially compressed Mn^{III} geometries with long $Mn-O_c$ equatorial bonds. In the IV/IV dimer, the ferromagnetic crossed exchange J_{yz/z^2} pathway partially cancels $J_{yz/yz}$ and, as a consequence, the antiferromagnetic $J_{xz/xz}$ pathway dominates the magnetic coupling. In the III/III dimer, the $J_{yz/yz}$ pathway is minimized due to the smaller Mn−O−Mn angle, and since the ferromagnetic J_{yz/z^2} pathway largely negates $J_{xz/xz}$, relatively weak overall antiferromagnetic coupling results. In the III/IV dimer, the structures involving high-spin and low-spin Mn^{III} are almost degenerate. In the high-spin case, the odd electron is localized on the Mn^{III} center, and the resulting antiferromagnetic coupling is similar to that found for the IV/IV dimer. In the alternative low-spin structure, the odd electron is significantly delocalized due to the crossed J_{yz/z^2} pathway, and cancellation between ferromagnetic and antiferromagnetic pathways leads to overall weak magnetic coupling. The delocalization partially converts the Mn^{IV} ion into high-spin Mn^{III}, and consequently, the spin ladders arising from coupling of Mn^{IV} ($S = 3/2$) with high-spin ($S = 2$) and low-spin ($S = 1$) Mn^{III} are configurationally mixed. Thus, in principle, the ground-state magnetic coupling in the mixed-valence dimer will involve contributions from three spin-ladders, two associated with the delocalized low-spin structure and the third arising from the localized high-spin structure.

Introduction

The rich redox chemistry of manganese enables it to play a central role in a variety of biologically important metalloproteins.[1−3] In particular, oxo−manganese clusters are either known or have been implicated in the catalytic function of manganese catalase,[3,4] manganese ribonucleotide reductase,[5,6] and the oxygen-evolving complex (OEC) of photosystem II.[7−10] To understand the structural, magnetic, and spectroscopic properties exhibited by these systems, numerous model complexes involving dinuclear and polynuclear mangenese clusters have been synthesized.[7−11] Most notably, since either oxo- or mixed oxo-carboxylato-bridged dinuclear manganese cores are postulated in the above biological systems, a number of model complexes containing these bridging groups have been structurally and magnetically characterized.[7−22,60,61] Essentially, these

* To whom correspondence should be addressed.

(1) Lawrence Que, J.; True, A. E. *Prog. Inorg. Chem.* **1990**, *38*, 97.
(2) Wieghardt, K. *Angew. Chem., Int. Ed. Engl.* **1989**, *28*, 1153.
(3) Dismukes, G. C. *Chem. Rev.* **1996**, *96*, 2909.
(4) Whittaker, M. M.; Barynin, V. V.; Antonyuk, S. V.; Whittaker, J. *Biochem.* **1999**, *38*, 9126.
(5) Willing, A.; Follmann, H.; Auling, G. *Eur. J. Biochem.* **1988**, *170*, 603.
(6) Willing, A.; Follmann, H.; Auling, G. *Eur. J. Biochem.* **1988**, *175*, 167.
(7) Manchanda, R.; Brudvig, G. W.; Crabtree, R. H. *Coord. Chem. Rev.* **1995**, *144*, 1.
(8) Yachandra, V. K.; Sauer, K.; Klein, M. P. *Chem. Rev.* **1996**, *96*, 2927.
(9) Pecoraro, V. L.; Baldwin, M. J.; Gelasco, A. *Chem. Rev.* **1994**, *94*, 807.
(10) Ruttinger, W.; Dismukes, G. C. *Chem. Rev.* **1997**, *97*, 1.
(11) Armstrong, W. H. In *Polynuclear Manganese Complexes as Models for the Photosystem II Water Oxidation Center*; Pecoraro, V. L., Ed.; VCH: Germany, 1992.
(12) Pal, S.; Chan, M. K.; Armstrong, W. H. *J. Am. Chem. Soc.* **1992**, *114*, 6398.
(13) Pal, S.; Armstrong, W. H. *Inorg. Chem.* **1992**, *31*, 5417.
(14) Pal, S.; Gohdes, J. W.; Christian, W.; Wilisch, A.; Armstrong, W. H. *Inorg. Chem.* **1992**, *31*, 713.
(15) Pal, S.; Olmstead, M. M.; Armstrong, W. H. *Inorg. Chem.* **1995**, *34*, 4708.

10.1021/ic0008767 CCC: $20.00
Published on Web 05/19/2001

Table 1. Experimental Structural Parameters in Manganese Dimers with a Di-μ-oxo-μ-carboxylato, or μ-oxo-di-μ-carboxylato Core and Terminal N Donor Ligands. O = Bridging Oxo Ligand, O_c = Carboxylate Oxygen. Tpen = *N,N,N′,N′*-Tetrakis(2-pyridylmethyl)1-2-ethanediamine, Bpea = *N,N,*-bis(2-pyridylmethyl) Ethylamine, Tacn = 1,4,7-triazacyclononane, Dtne = 1,2-bis(1,4,7-triazacyclonon-1-yl)ethane, Bpy = 2,2′-Bipyridine, Tmip = Tris(n-methylimidazol-2-yl)phosphine

			Mn−O/Å[b]		Mn−O_c/Å		Mn−N_{ax}/Å		Mn−N_{eq}/Å[b]		Mn−O−Mn/	
oxid'n state	ligand	Mn−Mn/Å	**III**	**IV**	**III**	**IV**	**III**	**IV**	**III**	**IV**	deg	ref
					$[Mn_2(\mu\text{-}O)_2(RCO_2)L_6]^{n+}$							
IV−IV	tpen	2.591		1.800		1.940		2.040		2.020	92.2	13
	bpea	2.580		1.799		1.942		1.986		2.042	91.6	12
	Me_4dtne	2.599		1.797		1.99		1.99		2.055	92.6	60
III−IV	tacn[a]	2.588	1.812	1.812	2.079	2.079	2.135	2.135	2.108	2.108	91.1	16
	tpen	2.591	1.832	1.784	2.196	1.940	2.072	2.057	2.225	2.062	91.5	14
	bpea	2.633	1.851	1.782	2.187	1.938	2.100	2.092	2.305	2.017	92.9	15
	dtne	2.553	1.830	1.782	2.142	1.971	2.205	2.095	2.074	2.076	89.9	60
	Me_4dtne[a]	2.574	1.814	1.806	2.068	2.051	2.148	2.141	2.094	2.096	90.6	60
					$[Mn_2(\mu\text{-}O)(RCO_2)_2L_6]^{n+}$							
III−IV	Me_3tacn	3.230	1.826	1.814	1.974	1.976	2.133	2.117	2.115	2.115	125.1	17
III−III	tacn	3.084	1.80		2.00		2.06		2.24		117.9	18
	Me_3tacn	3.084	1.81		2.047		2.131		2.232		120.9	18
	Me_3tacn	3.193	1.827		2.049		2.068		2.183		119.9	19
	bpy, N_3^-	3.153	1.802		2.087		2.092		2.132		124.3	20
	tmip	3.164	1.789		2.040		2.066		2.185		124.4	57
	tacn	3.096	1.788		2.062		2.066		2.183		119.9	21

[a] Mn^{III} and Mn^{IV} sites are indistinguishable due to structural disorder. [b] Average value.

model complexes can be separated into four different categories on the basis of the number and type of bridging groups, namely di-μ-oxo, di-μ-oxo μ-carboxylato, μ-oxo di-μ-carboxylato, and tri-μ-oxo bridged systems. The Mn−Mn distance and extent of magnetic coupling in these complexes varies enormously as the oxidation state and coordination of the manganese centers changes, from large Mn−Mn distances (>3 Å) and very weak antiferromagnetic (or even ferromagnetic) exchange in the case of μ-oxo di-μ-carboxylato bridged systems, to extremely short Mn−Mn distances (<2.3 Å) and strong antiferromagnetic coupling ($-J > 350$ cm^{-1}) for the tri-μ-oxo bridged systems.

Unfortunately, although there are numerous di-μ-oxo bridged complexes, only a few compounds exist with structures that contain $[Mn_2(\mu\text{-}O)_2(O_2CR)]^{n+}$ or $[Mn_2(\mu\text{-}O)(O_2CR)_2]^{n+}$ cores, none of which are known in all three of the oxidation states applicable to this study. Table 1 lists the relevant experimental bond distances for such complexes containing terminal nitrogen donor ligands in either $Mn^{IV}Mn^{IV}$, $Mn^{III}Mn^{IV}$, or $Mn^{III}Mn^{III}$ oxidation states. In general, a progressive increase in Mn−Mn distance and Mn−O−Mn angle with number of carboxylate groups present is observed. The limited structural data does not make it possible to reliably comment on the effect of oxidation state on the Mn−Mn distance, except that a 0.15 Å increase occurs when $[Mn^{III}_2(\mu\text{-}O)(O_2CH)_2(tacn)_2]^{2+}$ is oxidized to the $Mn^{III}Mn^{IV}$ state. No obvious trends are observed in the either the Mn−O or Mn−O_c bond distances with change in the bridge coordination; however, a difference of approximately 0.25 Å is found between the Mn^{III}−O_c and Mn^{IV}−O_c bonds in the mixed-valence $[Mn_2(\mu\text{-}O)_2(O_2CH)L_2]^{3+}$ (L = tpen, bpea) complexes, presumably the result of the axial elongation associated with Jahn−Teller active Mn^{III} centers. Smaller but consistent differences are also observed in the Mn^{III}−N_{ax} and Mn^{III}−N_{eq} bond distances, with the latter between 0.1 and 0.2 Å longer, again consistent with Jahn−Teller distorted high-spin Mn^{III} ions. However, it is noted that these bond length differences are the smallest or even absent in the complexes containing terminal tacn, Me_3tacn, dtne, and Me_4dtne donors, highlighting the rigidity of these ligands and their resistance to structural changes.

Several papers dealing with the electronic structure of manganese dimers with oxo and carboxylate bridges have appeared recently.[23−29,61,62] Of most significance is the detailed theoretical study by Noodleman and co-worker,[29] which employed DFT to investigate three crystallographically characterized Mn dimers involving terminal tacn ligands, namely $[Mn^{III}_2(\mu\text{-}O)(OAc)_2(tacn)_2]^{2+}$, $[Mn^{III}Mn^{IV}(\mu\text{-}O)(OAc)_2(tacn)_2]^{3+}$, and $[Mn^{III}Mn^{IV}(\mu\text{-}O)_2(OAc)\,(tacn)_2]^{2+}$. Since the focus of their study was on calculating the Heisenberg exchange coupling parameters and understanding the spin and charge distributions in the above systems, only single point calculations were performed, using the reported structures idealized to C_s symmetry. Several important results were obtained from their work; in particular, it was found that the Mn^{III} centers in the two mixed-valence III/IV dimers were low-spin, and in regard to delocalization, these dimers were best considered as Robin−Day class II complexes. Second, the calculations revealed the strong metal−ligand covalency existing in these systems as a result of the interaction of the Mn centers with the bridging oxo ligands. Strong covalency of the Mn-oxo bond was also

(16) Wieghardt, K.; Bossek, U.; Zsolnai, L.; Huttner, G.; Blondin, G.; Girerd, J.; Babonneau, F. *J. Chem. Soc., Chem. Commun.* **1987**, 651.
(17) Wieghardt, K.; Bossek, U.; Bonvoisin, J.; Beauvillain, P.; Girerd, J.; Nuber, B.; Weiss, J.; Heinze, J. *Angew. Chem., Int. Ed. Engl.* **1986**, *25*, 1030.
(18) Wieghardt, K.; Bossek, U.; Ventur, D.; Weiss, J. *J. Chem. Soc., Chem. Commun.* **1985**, 347.
(19) Bossek, U.; Hummel, H.; Weyhermuller, T.; Wieghardt, K.; Russell, S.; Vanderwolf, L.; Kolb, U. *Angew. Chem., Int. Ed. Engl.* **1996**, *35*, 1552.
(20) Vincent, J. P.; Tsai, H.; Blackman, A. G.; Wang, S.; Boyd, P. D. W.; Folting, K.; Huffman, J. C.; Lobkovsky, E. B.; Hendrickson, D. N.; Christou, G. *J. Am. Chem. Soc.* **1993**, *115*, 12353.
(21) Bossek, U.; Wieghardt, K.; Nuber, B.; Weiss, J. *Inorg. Chim. Acta* **1989**, *165*, 123.
(22) Bossek, U.; Weyhermuller, T.; Wieghardt, K.; Bonvoisin, J.; Girerd, J. J. *J. Chem. Soc., Chem. Commun.* **1989**, 633.
(23) Brunold, T. C.; Gamelin, D. R.; Stemmler, T. L.; Mandal, S. K.; Armstrong, W. H.; Pennerhahn, J. E.; Solomon, E. I. *J. Am. Chem. Soc.* **1998**, *120*, 8724.
(24) Siegbahn, P. E. M.; Crabtree, R. H. *J. Am. Chem. Soc.* **1999**, *121*, 117.
(25) Siegbahn, P. E. M.; Blomberg, M. R. A. *Annu. Rev. Phys. Chem.* **1999**, *50*, 221.
(26) McGrady, J. E.; Stranger, R. *J. Am. Chem. Soc.* **1997**, *119*, 8512.
(27) McGrady, J. E.; Stranger, R. *Inorg. Chem.* **1999**, *38*, 550.
(28) Delfs, C. D.; Stranger, R. *Inorg. Chem.* **2000**, *39*, 491.
(29) Zhao, X. G.; Richardson, W. H.; Chen, J. L.; Li, J.; Noodleman, L.; Tsai, H. L.; Hendrickson, D. N. *Inorg. Chem.* **1997**, *36*, 1198.

found in the more recent studies by Brunold et al.,[23,62] which reported single point DFT calculations on the complex $[Mn^{III}_2(\mu\text{-}O)(OAc)_2(Me_3tacn)_2]^{2+}$, and also the very recent DFT study by us on the tri-μ-oxo bridged complex $[Mn^{IV}_2(\mu\text{-}O)_3(NH_3)_6]^{2+}$.[28]

In earlier work, we presented a detailed analysis of the electronic structure and magnetic coupling in the model di-μ-oxo bridged dimer $[Mn_2(\mu\text{-}O)_2(NH_3)_8]^{n+}$ in three distinct oxidation states, $Mn^{IV}Mn^{IV}$, $Mn^{IV}Mn^{III}$, and $Mn^{III}Mn^{III}$, using a combination of DFT and the broken-symmetry approach.[26] In that study, the bidentate and tetradentate ligands which provided the terminal N donors in the structurally characterized systems were replaced with simple ammine ligands, allowing greater structural flexibility in the modeling. An important aspect of the study was that the geometry of the complex in the different oxidation states was allowed to optimize and thus respond to the differing electronic environments. The combination of these two effects led to enhanced Jahn−Teller distortions in the calculated structures for both the $Mn^{III}Mn^{III}$ and mixed-valence $Mn^{III}Mn^{IV}$ oxidation states, which impacted directly on both the extent and pathways of magnetic exchange. The importance of maintaining structural flexibility in the modeling of these types of systems was again highlighted in our recent DFT study of the peroxo-bridged $Mn^{IV}Mn^{IV}$ dimer $[Mn_2(\mu\text{-}O)_2(\mu\text{-}O_2)(NH_3)_6]^{2+}$.[27] Two-electron reduction of this complex to give the $Mn^{III}Mn^{III}$ dimer resulted in cleavage of the peroxo O−O bond and expulsion of the NH_3 ligand that was originally trans to the peroxo oxygen donor on each Mn center. In contrast, two-electron oxidation resulted in elimination of molecular oxygen. The dramatic changes in the geometry around the Mn centers upon both oxidation and reduction would have been significantly restricted or even prevented if less flexible ligands, such as tacn, were used in the modeling. The rigid nature of the tacn ligand is reflected in the reported structures of $[Mn^{III}_2(\mu\text{-}O)(OAc)_2(Me_3tacn)_2]^{2+}$, where there is at most only a 0.1 Å difference between the $Mn-N_{eq}$ and $Mn-N_{ax}$ distances, even though the Mn^{III} centers are high-spin and therefore subject to Jahn−Teller distortion.

In the following study, we present a detailed investigation of the electronic structure and geometry of the oxo- and carboxylato-bridged dimers $[Mn_2(\mu\text{-}O)_2(O_2CH)(NH_3)_6]^{n+}$ and $[Mn_2(\mu\text{-}O)(O_2CH)_2(NH_3)_6]^{n+}$ in three different oxidation states involving $Mn^{IV}Mn^{IV}$, $Mn^{III}Mn^{IV}$, and $Mn^{III}Mn^{III}$ cores. Particular attention is paid to the magnetic coupling present in these complexes and how it changes as a function of both the oxidation state and coordination environment of the manganese centers. For reasons outlined above, we have deliberately chosen to replace the ligands occurring in the structurally characterized systems with NH_3 donors in order to provide sufficient structural flexibility to adequately respond to changes in oxidation state. In this manner we hope to more faithfully reproduce the geometric changes that would occur for oxo- and carboxylato-bridged dimanganese cores in the biological systems.

As in previous studies completed by us[26−28] and other workers,[30−34] the electronic structure calculations are undertaken using a combination of approximate DFT and the broken-symmetry (BS) approach pioneered by Noodleman et al.[35] This methodology has been successfully used to describe the electronic structure of a large number of magnetically coupled transition metal systems,[30−34,36−39] including magnetically coupled centers in metalloproteins.[40−43] More recently, we have shown that incorporation of the BS methodology into DFT-based geometry optimization routines allows for the reproduction of the observed structures of metal dimer systems which encompass the entire range of metal−metal interactions, from weak magnetic coupling to multiple metal−metal bonding.[44−46] In the BS approach, the symmetry operations connecting the two metal centers are removed, thus allowing spin-up and spin-down electron density to localize on opposite sides of the molecule. In contrast, if the true molecular symmetry is imposed, the spin-up and spin-down density is forced to be distributed equally over both metal centers. This description of the magnetic electrons is appropriate in the delocalized limit where strong metal−metal bonding prevails, but is inadequate in the case where the magnetic coupling is weak. Thus, from the outset, the BS approach correctly models the antiferromagnetic state in magnetically coupled systems, and consequently, it has become accepted as a good representation of the nonorthogonal, natural magnetic orbitals in these systems.[30,32,47]

Computational Details and Methodology

The calculations reported here were performed using version 2.3.0 of the Amsterdam Density Functional (ADF) program[48] on Linux/Pentium II computers. Double-ζ basis sets (type III) which include a polarization function were used for N, O, and H, while a triple-ζ basis set (type IV) was employed for Mn. In the case of O and N, the 1s core orbitals were treated according to the frozen core approximation, while for Mn, core orbitals up to and including 3p were treated as frozen. All calculations of the highest possible spin state, S_{max}, were performed using the C_{2v} point group, whereas calculations using the BS approximation were performed using the C_s point group. The local density functional and local correlation and exchange potential of Vosko, Wilk, and Nusair[49] were used along with the gradient corrections of Beck[50] and Perdew[51] for exchange and correlation, respectively. Geometries were optimized using the algorithm of Versluis and Ziegler.[52]

(30) Bencini, A.; Totti, F.; Daul, C. A.; Doclo, K.; Fantucci, P.; Barone, V. *Inorg. Chem.* **1997**, *36*, 5022.
(31) Adamo, C.; Barone, V.; Bencini, A.; Totti, F.; Ciofini, I. *Inorg. Chem.* **1999**, *38*, 1996.
(32) Barone, V.; Bencini, A.; Ciofini, I.; Daul, C. A.; Totti, F. *J. Am. Chem. Soc.* **1998**, *120*, 8357.
(33) Cano, J.; Ruiz, E.; Alemany, P.; Lloret, F.; Alvarez, S. *J. Chem. Soc., Dalton Trans.* **1999**, 1669.
(34) Ruiz, E.; Cano, J.; Alvarez, S.; Alemany, P. *J. Comput. Chem.* **1999**, *20*, 1391.
(35) Noodleman, L. *J. Chem. Phys.* **1981**, *74*, 5737.
(36) Barone, V.; Bencini, A.; Cossi, M.; Dimatteo, A.; Mattesini, M.; Totti, F. *J. Am. Chem. Soc.* **1998**, *120*, 7069.
(37) Bencini, A.; Gatteschi, D.; Totti, F.; Sanz, D. N.; McCleverty, J. A.; Ward, M. D. *J. Phys. Chem.* **1998**, *102*, 10545.
(38) Cano, J.; Rodriguez-Fortea, A.; Alemany, P.; Alvarez, S.; Ruiz, E. *Chem. Eur. J.* **2000**, *6*, 327.
(39) Ruiz, E.; Cano, J.; Alvarez, S.; Alemany, P. *J. Am. Chem. Soc.* **1998**, *120*, 11122.
(40) Brunold, T. C.; Tamura, N.; Kitajima, N.; Morooka, Y.; Solomon, E. I. *J. Am. Chem. Soc.* **1998**, *120*, 5674.
(41) Brunold, T. C.; Solomon, E. I. *J. Am. Chem. Soc.* **1999**, *121*, 8288.
(42) Brunold, T. C.; Solomon, E. I. *J. Am. Chem. Soc.* **1999**, *121*, 8277.
(43) Noodleman, L.; Case, D. A. *Adv. Inorg. Chem.* **1992**, *38*, 423.
(44) McGrady, J. E.; Lovell, T.; Stranger, R. *Inorg. Chem.* **1997**, *36*, 3242.
(45) McGrady, J. E.; Stranger, R.; Lovell, T. *J. Phys. Chem. A* **1997**, *101*, 6265.
(46) McGrady, J. E.; Stranger, R.; Lovell, T. *Inorg. Chem.* **1998**, *37*, 3802.
(47) Kahn, O. *Molecular Magnetism*; VCH Publishers: New York, 1993.
(48) Baerends, E. J.; Bérces, A.; Bo, C.; Boerrigter, P. M.; Cavallo, L.; Deng, L.; Dickson, R. M.; Ellis, D. E.; Fan, L.; Fischer, T. H.; Fonseca Guerra, C.; van Gisbergen, S. J. A.; Groeneveld, J. A.; Gritsenko, O. V.; Harris, F. E.; van den Hoek, P.; Jacobsen, H.; van Kessel, G.; Kootstra, F.; van Lenthe, E.; Osinga, V. P.; Philipsen, P. H. T.; Post, D.; Pye, C.; Ravenek, W.; Ros, P.; Schipper, P. R. T.; Schreckenbach, G.; Snijders, J. G.; Sola, M.; Swerhone, D.; te Velde, G.; Vernooijs, P.; Versluis, L.; Visser, O.; van Wezenbeek, E.; Wiesenekker, G.; Wolff, S. K.; Woo, T. K.; Ziegler, T. Amsterdam Density Functional, 1999.

Calculation of magnetic exchange constants was based on the BS approach, developed by Noodleman,[35] for the weakly coupled limit. In the spin Hamiltonian formalism, the magnetic exchange between two interacting spin centers S_1 and S_2 is written as

$$H = -2JS_1 \cdot S_2 \quad (1)$$

where J is the magnetic exchange constant. The coupling of the two spin centers results in a series of states (spin ladder) with total spin S in the range $|S_1 - S_2| \leq S \leq S_1 + S_2$ and relative energies given by

$$E(S) = -JS(S+1) \quad (2)$$

Noodleman has shown that the exchange constant can be obtained from the energy difference between the BS and maximum spin (S_{max}) states via the expression

$$-J = \frac{E(S_{max}) - E_{BS}}{S_{max}^2} \quad (3)$$

This energy difference can be determined using DFT, as both the BS and S_{max} states are described by single determinant wave functions. The energies used in eq 3 correspond to the optimized geometries of the BS and S_{max} states. In the case of mixed-valence systems, the above spin Hamiltonian must be modified to take account of the resonance delocalization (double exchange) between the two metal centers. For a completely delocalized system, the appropriate expression is

$$H = -2JS_1 \cdot S_2 \pm B(S + {}^1/_2) \quad (4)$$

where B is the resonance delocalization parameter which results in a splitting of each of the total spin states into symmetric and antisymmetric components. The value of B may be calculated using the expression

$$E(S_{max})_u - E(S_{max})_g = 2B(S_{max} + {}^1/_2) \quad (5)$$

where $E(S_{max})_u$ and $E(S_{max})_g$ are the energies of the two delocalized high-spin states corresponding to the unpaired electron occupying the symmetric (g) and antisymmetric (u) combinations of the magnetic orbitals involved in the delocalization, respectively. The exchange coupling constant is then obtained from

$$E(S_{max}) - E_{BS} = -J(S_{max} + {}^1/_2)(S_{max} - {}^1/_2) \quad (6)$$

where the value of $E(S_{max})$ in this expression corresponds to the average of $E(S_{max})_u$ and $E(S_{max})_g$. It is important to note that significant resonance delocalization can result in the ground-state being S_{max} even when the overall exchange coupling is antiferromagnetic. In the localized limit, the value of J can also be calculated from eq 6 by replacing $E(S_{max})$ with the energy of the high-spin state, either $E(S_{max})_u$ or $E(S_{max})_g$, whichever lies at the lowest energy.

Results and Discussion

In the following discussion, we will describe separately the calculated geometry and electronic structure of the di-μ-oxo-carboxylato and μ-oxo-di-carboxylato dimanganese systems in $Mn^{IV}Mn^{IV}$, $Mn^{III}Mn^{III}$, and $Mn^{III}Mn^{IV}$ oxidation states. This will be followed by discussion of the major redox-induced changes in the geometry and electronic structure of each bridging system, and the resulting implications for magnetic coupling. Finally, the overall effect of progressively replacing the oxo bridges with carboxylate ligands will be considered.

$[Mn_2(\mu\text{-}O)_2(O_2CH)(NH_3)_6]^{n+}$. IV/IV Dimer. From the data given in Table 2 , it is apparent that the calculated geometry of the IV/IV dimer $[Mn_2(\mu\text{-}O)_2(O_2CH)(NH_3)_6]^{3+}$ is mostly in agreement with the reported crystal structures. However, the calculated Mn−Mn distance is approximately 0.17 Å longer, and consequently the Mn−O−Mn angle is approximately 5° larger, compared to the known structures. A possible cause of this discrepancy is that the terminal ligands for the complexes given in Table 1 contain either unsaturated or cyclically constrained N donors. The remaining structural parameters, such as the Mn−O, Mn−O_c, and Mn−N distances, are in reasonable agreement with the experimental values. The calculated Mn−N_{eq} distance is slightly longer than the Mn−N_{ax} distance, and presumably this difference can be attributed to the trans influence of the oxo ligands.

Table 2. Calculated Structural Parameters for the $[Mn_2(\mu\text{-}O)_2(HCO_2)(NH_3)_6]^{n+}$ and $[Mn_2(\mu\text{-}O)(HCO_2)_2(NH_3)_6]^{n+}$ Series of Compounds

	IV−IV		III−IV		III−III	
	BS	**S = 3**	**BS**	**S = 7/2**	**BS**	**S = 4**
			$[Mn_2(\mu\text{-}O)_2(HCO_2)(NH_3)_6]^{n+}$			
Mn−Mn/Å	2.738	2.708	2.667	2.691	2.595	2.645
Mn^{IV}−O/Å	1.825	1.841	1.805	1.806		
Mn^{III}−O/Å			1.836	1.890	1.832	1.855
Mn^{IV}−O_c/Å	1.994	1.965	2.004	2.006		
Mn^{III}−O_c/Å			2.156	2.192	2.321	2.320
Mn^{IV}−N_{ax}/Å	2.109	2.112	2.118	2.126		
Mn^{III}−N_{ax}/Å			2.352	2.466	2.446	2.479
Mn^{IV}−N_{eq}/Å	2.166	2.168	2.186	2.206		
Mn^{III}−N_{eq}/Å			2.203	2.178	2.215	2.207
O−Mn^{IV}−O/°	80.4	83.0	84.1	86.5		
O−Mn^{III}−O/°			82.4	81.8	85.3	84.5
Mn−O−Mn/°	97.2	94.7	94.2	93.4	90.2	90.9
Mn−O−O−Mn/°	21	22	23	22	31	31
			$[Mn_2(\mu\text{-}O)(HCO_2)_2(NH_3)_6]^{n+}$			
Mn−Mn/Å	3.304	3.312	3.269	3.248	3.179	3.163
Mn^{IV}−O/Å	1.800	1.848	1.784	1.799		
Mn^{III}−O/Å			1.817	1.867	1.802	1.818
Mn^{IV}−O_c/Å	1.960	1.954	1.943	1.970		
Mn^{III}−O_c/Å			2.121	2.074	2.106	2.100
Mn^{IV}−N_{ax}/Å	2.134	2.161	2.179	2.181		
Mn^{III}−N_{ax}/Å			2.115	2.141	2.149	2.164
Mn^{IV}−N_{eq}/Å	2.119	2.120	2.133	2.176		
Mn^{III}−N_{eq}/Å			2.277	2.244	2.302	2.309
Mn−O−Mn/°	133.2	127.4	130.5	124.7	123.8	120.9

Before discussing the electronic structure of the d^3d^3 complex $[Mn_2(\mu\text{-}O)_2(O_2CH)(NH_3)_6]^{3+}$, it is convenient to define a local coordinate system for each Mn ion which will apply to all three oxidation states. Accordingly, the z axis at each Mn center is chosen such that it is parallel to the appropriate Mn−O_c bond axis, and the y axis is defined so that the Mn−Mn vector lies in the yz plane, as shown in Figure 1. Using this definition, the octahedral t_{2g} orbitals on each Mn center correspond to $d_{x^2-y^2}$, d_{yz}, and d_{xz}, and the e_g orbitals to d_{z^2} and d_{xy}. Low symmetry distortions, such as the nonequivalence of N and O donors, the long Mn−O_c bonds, and small O−Mn−O angle, remove the degeneracy of the parent t_{2g} and e_g orbitals. In the BS calculation, the full dimer symmetry of C_{2v} is reduced to C_s, with the result that the occupied t_{2g} based $d_{x^2-y^2}$ and d_{yz} orbitals transform as a′ representations and d_{xz} as a″, while the unoccupied e_g orbitals, d_{z^2} and d_{xy}, transform as a′ and a″, respectively. Thus, the BS configuration can be written as $(26a'\uparrow)^1(26a'\downarrow)^1(27a'\uparrow)^1(27a'\downarrow)^1(17a''\uparrow)^1(17a''\downarrow)^1$, corresponding to singly occupied sets of t_{2g} orbitals, one which is spin-up (↑) and localized on Mn_1 and the other which is spin-down (↓) and localized on Mn_2. From Figure 2, the spin-up components of the t_{2g} orbitals on Mn_1 are the lowest in energy and are therefore occupied, but in Mn_2 the corresponding spin-down orbitals lie at the lowest energy. On both Mn centers, the occupied majority

(49) Vosko, S. H.; Wilk, L.; Nusair, M. *Can. J. Phys.* **1980**, *58*, 1200.
(50) Becke, A. D. *Phys. Rev. A* **1988**, *38*, 3098.
(51) Perdew, J. P. *Phys. Rev. B* **1986**, *33*, 8822.
(52) Versluis, L.; Ziegler, T. J. *J. Chem. Phys.* **1988**, *88*, 322.

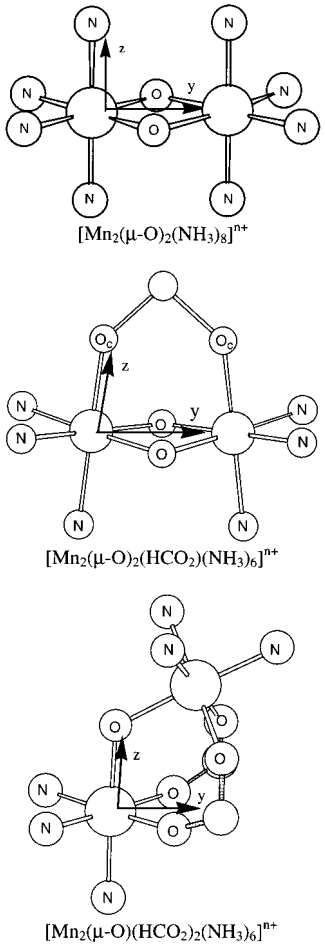

Figure 1. Structures and metal-based coordinate systems for $[Mn_2(\mu\text{-}O)_2(NH_3)_8]^{n+}$, $[Mn_2(\mu\text{-}O)_2(HCO_2)(NH_3)_6]^{n+}$, and $[Mn_2(\mu\text{-}O)(HCO_2)_2(NH_3)_6]^{n+}$ complexes.

spin t_{2g} orbitals 26a′ ($d_{x^2-y^2}$), 27a′ (d_{yz}), and 17a″ (d_{xz}) are stabilized by approximately 2 eV over their vacant minority spin counterparts (28a′, 18a″, and 29a′) by spin polarization. The majority spin e_g orbitals 30a′ (d_{z^2}) and 19a″ (d_{xy}) are located 2.8 eV above the 17a″ HOMO, and their minority spin counterparts (31a′ and 20a″) are an additional 0.8 eV higher in energy.

Given that O^{2-} is a strong donor,[23,26,29] the ligand field in $[Mn_2(\mu\text{-}O)_2(O_2CH)(NH_3)_6]^{3+}$ is equivalent to a tetragonal elongation with the *z* axis parallel to the Mn−O_c bond. The splitting of the minority spin e_g orbitals shown in Figure 2 clearly reflects this conclusion, in that the d_{z^2} (31a′) orbital is 0.5 eV lower in energy than d_{xy} (20a″). This rather simple analysis ignores the metal−ligand π interactions, which is evident from the fact that the $d_{x^2-y^2}$ orbital is lower in energy than d_{xz} and d_{yz}, contrary to expectations for a tetragonally elongated field which would normally stabilize the d_{xz} and d_{yz} orbitals relative to $d_{x^2-y^2}$. The fact that the opposite situation occurs in $[Mn_2(\mu\text{-}O)_2(O_2CH)(NH_3)_6]^{3+}$ can be largely attributed to π interactions between Mn and the oxo bridges on the basis of the significant contributions the oxo ligands make to the 26a′, 27a′, and 17a″ levels in Table 3. Strong Mn−oxo π interactions have been observed in other calculations on μ-oxo bridged Mn dimers[23,29,62] and were recently proposed by us as the principal mechanism for the strong antiferromagnetic exchange in $[Mn_2(\mu\text{-}O)_3(NH_3)_6]^{2+}$.[28]

Having described the electronic structure of the complex largely from the perspective of the metal−ligand interactions, it is now appropriate to examine in detail the nature of the metal−metal interactions. In the discussion to follow, we will focus on the spin-up magnetic orbitals, as their spin-down counterparts are simply related by a reflection plane that contains the two oxo bridges and is normal to the Mn−Mn axis. Since the tilt of the Mn_2O_2 core (defined by the deviation of Mn_2 out of the O−Mn_1−O plane) is relatively small, 20°, it is reasonable to expect that the metal−metal interaction in $[Mn_2(\mu\text{-}O)_2(O_2CH)(NH_3)_6]^{3+}$ will be similar to that in the planar Mn(μ-$O)_2$Mn system which we have studied previously. Consequently, the direct metal−metal interactions can be categorized as σ, π, and δ in nature, arising from the overlap of $d_{x^2-y^2}$, d_{yz}, and d_{xz} orbitals on opposite Mn centers, respectively. However, direct metal−metal interactions are in fact small, as is evident from the contour plots of the 26a″↑, 27a″↑, and 17a″↑ orbitals shown in Figure 3, due to the moderately large Mn−Mn distances (∼2.7 Å) and the contracted nature of the 3d orbitals on the Mn^{IV} ions. Therefore, analogous to the di-μ-oxo bridged complex $[Mn_2(\mu\text{-}O)_2(NH_3)_8]^{3+}$, the magnetic coupling is dominated by superexchange via the bridging ligands. [26,28] Due to the low symmetry, C_s, there are a large number of possible superexchange pathways, but fortunately, only a small number of these make a significant contribution to the overall magnetic exchange. Of the symmetric exchange pathways, denoted

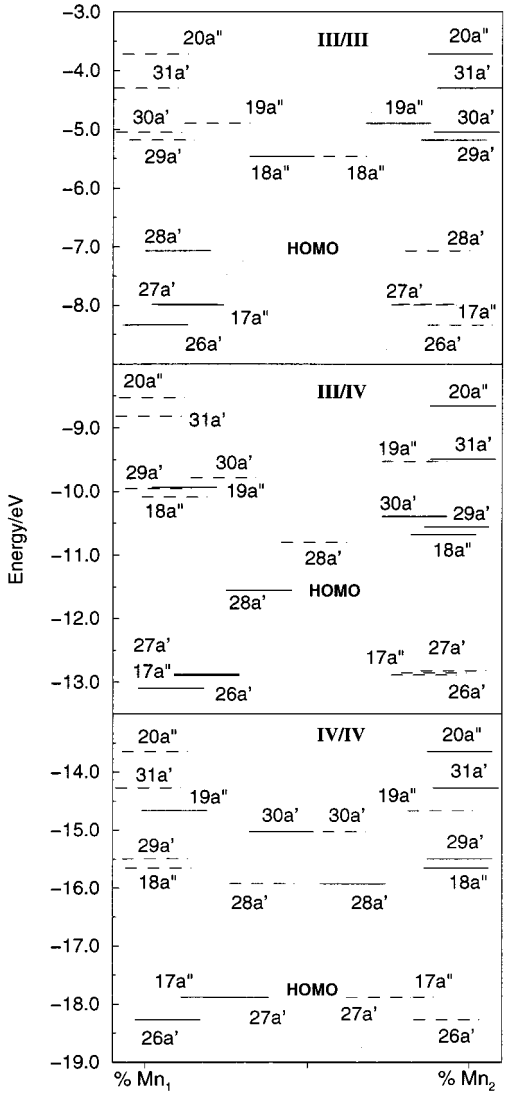

Figure 2. Energies and delocalization of the metal-based orbitals obtained from broken-symmetry calculations for $[Mn_2(\mu\text{-}O)_2(HCO_2)(NH_3)_6]^{n+}$ in the $Mn^{IV}Mn^{IV}$, $Mn^{III}Mn^{IV}$, and $Mn^{III}Mn^{III}$ oxidation states.

Table 3. Mulliken Decomposition of the Essentially Mn Based Molecular Orbitals into Contributions from the Mn and Bridging Ligands for the IV/IV, III/IV, and III/III Dimers of $[Mn_2(\mu\text{-}O)_2(HCO_2)(NH_3)_6]^{n+}$. Atomic Orbital Contributions to Molecular Orbitals Are Listed in Order of Weighting. Only Spin-up Orbitals Are Listed for IV/IV and III/III Dimers

MO	energy/eV	occ	Mn_1	Mn_2	O	O_c	N
			$[Mn_2(\mu\text{-}O)_2(HCO_2)(NH_3)_6]^{3+}$				
26a′↑	−18.262	2	60 $d_{x^2-y^2}$	5 d_{z^2}, $d_{x^2-y^2}$	27	1	5
27a′↑	−17.889	2	37 d_{yz}	14 d_{yz}, d_{z^2}	28	10	5
17a″↑	−17.878	2	29 d_{xz}	8 d_{xz}	44	14	2
28a′↑	−15.921	0	27 d_{z^2}	48 $d_{x^2-y^2}$	2	7	11
18a″↑	−15.660	0	3	76 d_{xz}	16	2	2
29a′↑	−15.494	0	2	75 d_{yz}	18	1	1
30a′↑	−15.033	0	27 d_{z^2}	38 $d_{x^2-y^2}$	16	6	7
19a″↑	−14.671	0	49 d_{xy}	4 d_{xy}, d_{xz}	32	0	12
31a′↑	−14.279	0	1	66 d_{z^2}	7	9	12
20a″↑	−13.656	0	1	63 d_{xy}	22	0	11
			$[Mn_2(\mu\text{-}O)_2(HCO_2)(NH_3)_6]^{2+}$				
26a′↑	−13.117	1	64 $d_{x^2-y^2}$	6	24	1	3
17a″↑	−12.852	1	50 d_{xz}	11 d_{xz}	27	9	0
27a′↑	−12.798	1	55 d_{yz}	13 d_{xz}, d_{z^2}	22	3	5
17a″↓	−12.699	1	6 d_{xz}	52 d_{xz}	29	10	0
26a′↓	−12.663	1	9 d_{yz}, $d_{x^2-y^2}$	56 d_{yz}, $d_{x^2-y^2}$	23	6	2
27a′↓	−12.591	1	3	69 $d_{x^2-y^2}$, d_{yz}	23	0	4
28a′↑	−11.505	1	44 d_{z^2}	24 $d_{x^2-y^2}$	1	14	12
28a′↓	−10.927	0	37 $d_{x^2-y^2}$	40 d_{z^2}	1	10	11
18a″↑	−10.794	0	6 d_{xy}	68 d_{xz}	20	1	1
29a′↑	−10.652	0	3	72 d_{yz}	19	2	1
30a′↑	−10.451	0	13 d_{z^2}	63 $d_{x^2-y^2}$	17	2	2
18a″↓	−10.308	0	75 d_{xz}	8 d_{xy}, d_{xz}	13	1	2
29a′↓	−10.181	0	78 d_{yz}, $d_{x^2-y^2}$	4	14	0	1
19a″↑	−10.022	0	48 d_{xy}	7 d_{xz}	32	0	10
30a′↓	−9.995	0	56 $d_{x^2-y^2}$	18 d_{z^2}	14	4	2
19a″↓	−9.596	0	10 d_{xz}	49 d_{xy}	28	0	8
31a′↑	−9.378	0	1	68 d_{z^2}	7	9	9
31a′↓	−8.945	0	77	1	4	7	7
20a″↑	−8.552	0	1	65 d_{xy}	21	0	8
20a″↓	−8.486	0	69	1	19	0	8
			$[Mn_2(\mu\text{-}O)_2(HCO_2)(NH_3)_6]^{+}$				
26a′↑	−8.332	2	60 $d_{x^2-y^2}$	3	30	2	1
27a′↑	−7.985	2	55 d_{yz}	7 d_{yz}	28	2	4
17a″↑	−7.988	2	47 d_{xz}	7 d_{xz}	39	4	0
28a′↑	−7.069	2	55 d_{z^2}	6 $d_{x^2-y^2}$	4	20	8
18a″↑	−5.459	0	38 d_{xy}	27 d_{xz}	24	0	5
29a′↑	−5.177	0	4	80 $d_{x^2-y^2}$	11	0	0
30a′↑	−5.048	0	1	85 d_{yz}	11	0	0
19a″↑	−4.892	0	16 d_{xy}	59 d_{xz}	19	0	2
31a′↑	−4.297	0	0	78 d_{z^2}	3	5	2
20a″↑	−3.713	0	2	66 d_{xy}	19	0	4

$J_{x^2-y^2/x^2-y^2}$, $J_{xz/xz}$, and $J_{yz/yz}$, depicted in Figure 4, only $J_{xz/xz}$ and $J_{yz/yz}$ will form efficient pathways due to the overlap of the d_{xz} and d_{yz} orbitals with the relevant out-of-plane pπ orbitals of the oxo bridging ligands. In the case of the $J_{x^2-y^2/x^2-y^2}$ pathway, the in-plane pπ orbitals of the oxo ligands are optimized for overlap with one Mn center but are nearly orthogonal to the other Mn center. Accordingly, magnetic interactions via this symmetric pathway are unlikely to be efficient. These arguments are supported by the orbital compositions given in Table 3, where it is seen that the 27a′ and 17a″ levels are partially delocalized over both Mn centers with Mn_1:Mn_2 ratios of 37:14 and 29:8, respectively, whereas the 26a′ level, with a ratio of 60:5, is essentially localized on one Mn center. From the negligible O_c contribution on Mn_2 to these orbitals, it can be concluded that superexchange interactions via the bridging carboxylate ligands are minimal. Overall, the calculated spin density of ±2.75 on the Mn ions is indicative of relatively weak antiferromagnetic coupling given that most of the reduction from a net spin value of ±3.0 can be attributed to covalent interactions with the ligands.

From symmetry arguments, any orbitals that belong to the same irreducible representation may overlap and, therefore, give rise to a possible superexchange interaction. Thus, in addition to symmetric pathways involving the same d orbital on both metal centers, it is possible to have crossed-exchange pathways where the orbital on one metal center is different from that on the opposite center. This is illustrated by the $J_{x^2-y^2/z^2}$ pathway shown in Figure 4. Since both the $d_{x^2-y^2}$ and d_{z^2} orbitals have a′ symmetry, they can interact; this occurs either through direct overlap or via overlap with the in-plane pπ orbitals of the oxo ligands. In either case, the $d_{x^2-y^2}$ orbital on one metal center interacts with the torus of the d_{z^2} orbital on the other. In fact, from Table 3 and the contour plot for 26a′ in Figure 3, it is apparent that the Mn_2 contribution to this level comprises both d_{z^2} and $d_{x^2-y^2}$ orbitals, and therefore, the symmetric $J_{x^2-y^2/x^2-y^2}$ pathway is mixed with the crossed-exchange $J_{x^2-y^2/z^2}$ pathway. Although the orientation of the $d_{x^2-y^2}$, d_{z^2}, and in-plane oxo pπ orbitals is favorable for superexchange, this pathway turns out not to be efficient in both the occupied 26a′ and vacant 31a′ orbitals, due to the combined effect of the ligand-field and spin-polarization splittings which result in a relatively large energetic separation of the majority spin $d_{x^2-y^2}$ and minority spin d_{z^2} orbitals on opposite Mn centers. In contrast, the unoccupied 28a′ and 30a′ levels are significantly delocalized, with Mn_1:Mn_2 ratios of 27:48 and 27:38, respectively. For these orbitals, the combined effect of the ligand-field and spin-polarization splittings now act to reduce the energetic separation of the majority spin d_{z^2} and minority spin $d_{x^2-y^2}$ orbitals on opposite centers. Although the 28a′ LUMO has no bearing on the charge distribution in the complex, it is presumably this orbital that is occupied upon reduction, and therefore, the possibility exists of significant delocalization of the odd electron in the analogous mixed-valence complex. In principle, it is possible to observe other crossed-exchange pathways involving orbitals of the same symmetry, namely $J_{x^2-y^2/yz}$, $J_{z^2/yz}$, and $J_{xy/xz}$. Fortunately, the present calculations indicate that these crossed-exchange pathways do not make significant contributions to the magnetic coupling in $[Mn_2(\mu\text{-}O)_2(O_2CH)(NH_3)_6]^{3+}$, but this may not be the case if the tilt of the Mn_2O_2 core is increased.

III/III Dimer. Currently, no complexes involving a $[Mn_2(\mu\text{-}O)_2(O_2CR)]^{n+}$ core in the III/III oxidation state have been structurally characterized. However, based on the structural parameters for $[Mn_2(\mu\text{-}O)_2(O_2CH)(NH_3)_6]^{1+}$ given in Table 2, there are a number of important differences between the calculated structures for the III/III and IV/IV oxidation states. First, the calculated Mn−Mn distance of 2.595 Å for the III/III dimer is 0.14 Å shorter, and the Mn−O−Mn and O−Mn−O angles of 90° and 85° are 7° smaller and 5° larger, respectively, all consistent with a more compressed geometry of the Mn_2O_2 core. This compressed structure also results in a greater tilting of the Mn_2O_2 core, 31° compared to 21° in the IV/IV dimer. The most dramatic differences, however, are seen in the Mn−N and Mn−O_c bond distances. In particular, the Mn−N_{ax} and Mn−O_c bonds have increased by over 0.33 and 0.34 Å, respectively, in the reduced complex.

As was anticipated earlier, two electron reduction from the IV/IV to the III/III oxidation state sees the two extra electrons occupying the (28a′↑) and (28a′↓) orbitals, resulting in the BS configuration $(26a'\uparrow)^1(26a'\downarrow)^1(27a'\uparrow)^1(27a'\downarrow)^1(17a''\uparrow)^1(17a''\downarrow)^1(28a'\uparrow)^1(28a'\downarrow)^1$. From Figure 2, the relative energies of the 26a′, 17a″, and 27a′ orbitals do not change substantially in going from the IV/IV to the III/III dimer, and the contribution (Table 3) of the bridging oxo pπ orbitals to these levels remains large, in the vicinity of 25−40%. The composition of the 28a′ HOMO

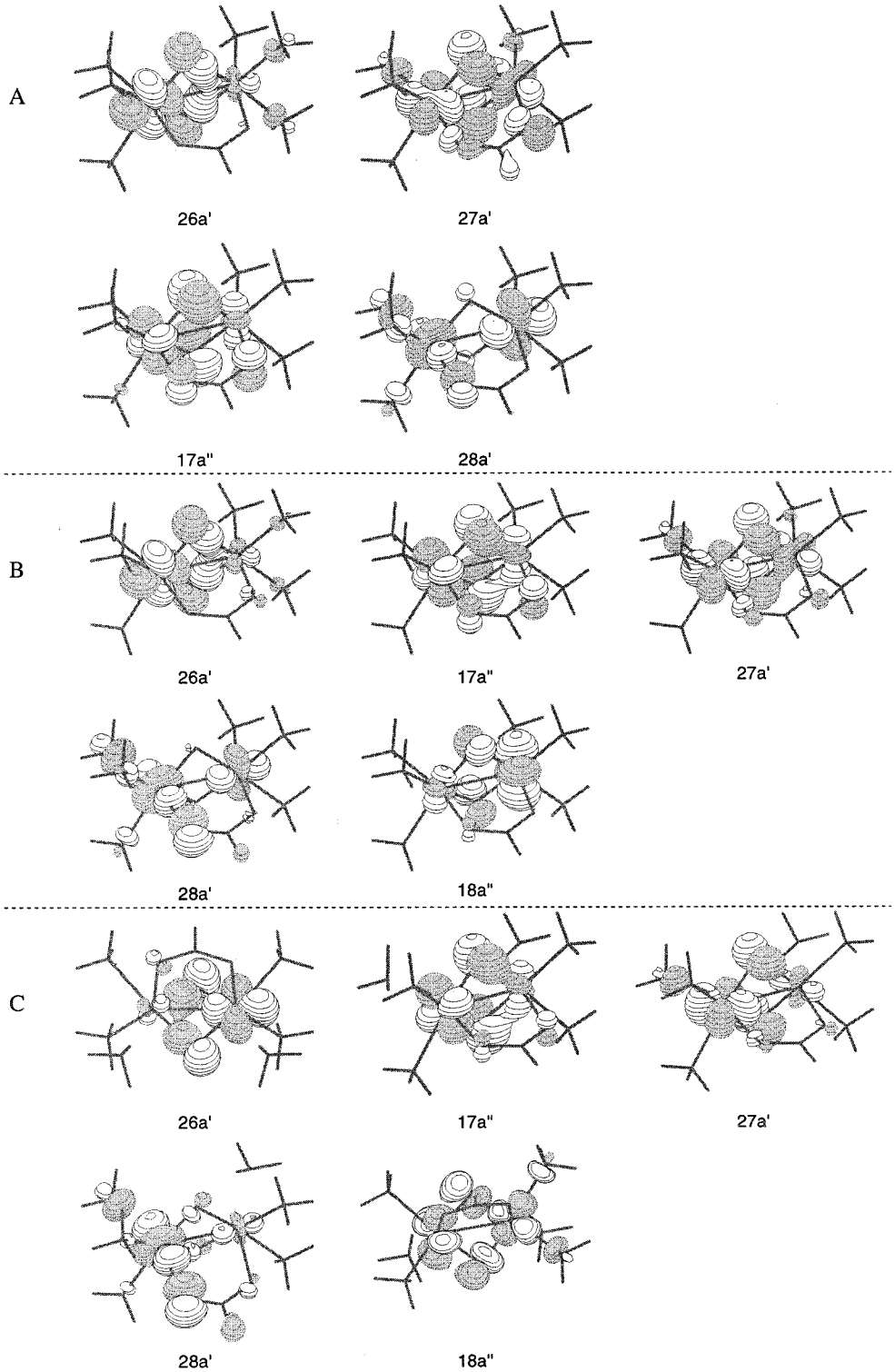

Figure 3. Surface plots of the Mn based occupied MOs and LUMO obtained from broken-symmetry calculations on (a) $[Mn_2(\mu\text{-}O)_2(HCO_2)(NH_3)_6]^{3+}$, (b) $[Mn_2(\mu\text{-}O)_2(HCO_2)(NH_3)_6]^{2+}$, and (c) $[Mn_2(\mu\text{-}O)_2(HCO_2)(NH_3)_6]^{1+}$.

indicates that the extra electrons have entered the majority spin e_g based d_{z^2} orbital on each metal, and therefore, the Mn^{III} ions adopt a high-spin configuration. The high-spin nature of the metal ions is also reflected in the calculated net spin density of ± 3.61 on the Mn centers, the reduction from ± 4.0 being reasonably attributed to metal−ligand covalency effects. Since the nearest minority spin t_{2g} based orbital, 29a′ ($d_{x^2-y^2}$), lies approximately 1.9 eV higher in energy, the high-spin configuration is significantly stabilized over the low-spin alternative. It should be pointed out that the BS calculation does not force the Mn centers to adopt a high-spin or low-spin configuration as the highest occupied a′ levels can correspond to either majority spin or minority spin orbitals. Since the 28a′ HOMO is antibonding with respect to the N_{ax} and O_c donors, both the $Mn-N_{ax}$ and $Mn-O_c$ bonds are notably longer than those in the IV/IV dimer, consistent with the axial elongation of high-spin Mn^{III} ions due to the Jahn−Teller effect. The axial distortion results in a substantial splitting (∼1.6 eV) for the majority spin e_g orbitals, 28a′ and 18a″.

On the basis of the contour plots for the 26a′↑, 27a′↑ and 17a″↑

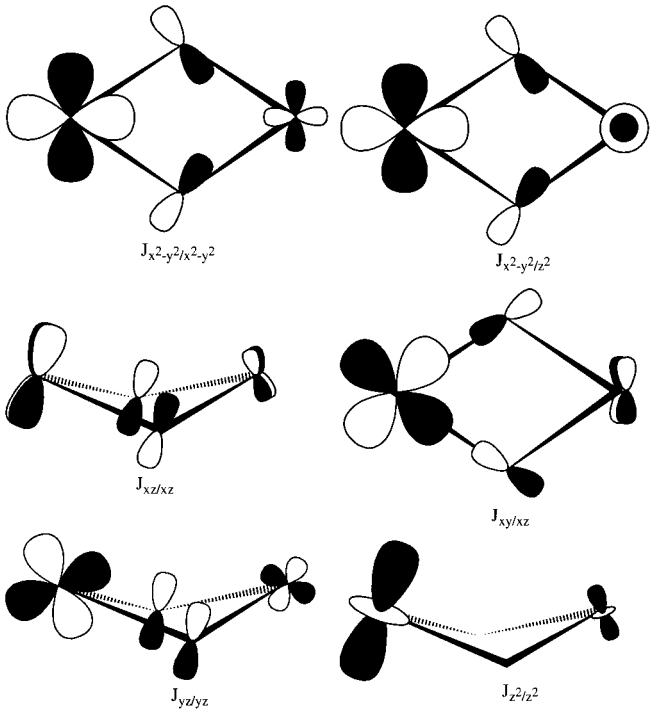

Figure 4. Schematic representation of the main exchange pathways in $[Mn_2(\mu\text{-}O)_2(HCO_2)(NH_3)_6]^{n+}$ complexes.

orbitals shown in Figure 3, and the large contributions of the bridging oxo ligands to these levels shown in Table 3, the magnetic coupling in the III/III dimer is largely determined by superexchange interactions. The Mn_1:Mn_2 delocalization ratios of 55:7 and 47:7 for the 27a′ and 17a″ levels indicate that the symmetric exchange pathways $J_{xz/xz}$ and $J_{yz/yz}$ again dominate the magnetic coupling within the t_{2g} set of orbitals. The delocalization of the 28a′ HOMO (55:6), although comparable to that of 27a′, is markedly reduced compared to the same level in the IV/IV dimer where the delocalization ratio was 27:48. The reduction can be mostly attributed to the ineffectiveness of the crossed exchange $J_{x^2-y^2/z^2}$ pathway in the III/III dimer. This situation arises because the small axial ligand field on one Mn center (due to the long axial Mn−O_c and Mn−N_{ax} bonds) and large spin-polarization splitting of the t_{2g} levels on the other result in a relatively large energetic separation of the majority spin d_{z^2} and minority spin $d_{x^2-y^2}$ orbitals on opposite metal centers. Given the moderate contribution (∼20%) of the carboxylate O donors to the 28a′ orbital, the question arises as to whether the symmetric J_{z^2/z^2} pathway, involving superexchange via the bridging carboxylate ligand, is important in the III/III dimer. However, the breakdown of the carboxylate contribution to 28a′ reveals that 19% is localized on O_c coordinated to Mn_1, and only 1% is localized on O_c coordinated to Mn_2. The small delocalization of the 28a′ level across both carboxylate oxygens is also evident from the contour plot of this orbital shown in Figure 3. Therefore, it is reasonable to assume that superexchange via the carboxylate bridge is negligible.

In stark contrast with the relatively small delocalization of the occupied 26a′, 27a′, 28a′, and 17a″ levels, the 18a″ LUMO is significantly delocalized between the two Mn centers. From the composition of this level (38% d_{xy} on Mn_1 and 27% d_{xz} on Mn_2) and its contour plot in Figure 3, it is clear that the crossed-exchange $J_{xy/xz}$ pathway is largely responsible for the delocalization. This pathway is depicted in Figure 4 and involves overlap of the d_{xy} and d_{xz} orbitals on opposite Mn centers with the in-plane pπ orbitals of the bridging oxo ligands. In the planar Mn_2O_2 limit, this pathway is not possible on symmetry grounds, but as the tilt of the Mn_2O_2 core increases, this superexchange pathway becomes viable.

III/IV Dimer. With the exception of the Mn−O and Mn−N_{eq} bond distances, which are similar for both Mn^{III} and Mn^{IV} sites, the remaining structural data in Table 2 indicate that the coordination environments of the Mn^{III} and Mn^{IV} centers in the III/IV dimer are appreciably different, symptomatic of a trapped valence system. In particular, the Mn^{III}−N_{ax} and Mn^{III}−O_c bonds are approximately 0.25 and 0.15 Å longer than their Mn^{IV} counterparts, indicative of a Jahn−Teller distorted, high-spin Mn^{III} site with the unpaired electron occupying the d_{z^2} orbital. However, both the Mn^{III}−N_{ax} and Mn^{III}−O_c bonds are somewhat shorter than those in the III/III dimer, suggesting that the odd electron is not completely localized on the Mn^{III} center. The structural data for the Mn^{IV} site, on the other hand, is very similar to that calculated for the IV/IV dimer, implying that any delocalized electron density originating from the Mn^{III} site is transferred to an orbital on Mn^{IV} that is essentially nonbonding. Based on the data in Table 1, the Mn^{III} site in the reported structure of the mixed-valence complex $[Mn_2(\mu\text{-}O)_2(OAc)(tacn)_2]^{2+}$ does not appear to undergo any significant Jahn−Teller distortion. Although this conclusion is consistent with the calculations of Noodleman and co-workers, which predicted a low-spin Mn^{III} configuration, establishing the absence of the Jahn−Teller effect in this complex is difficult because, due to structural disorder, only averaged Mn−N_{ax} and Mn−O_c bond distances were used. In contrast, in the mixed-valence structures reported by Pal et al.,[13−15] comprising a mixture of amine- and pyridine-like terminal ligands, it is quite clear that the Mn^{III} sites undergo significant Jahn−Teller distortion as the Mn^{III}−O_c bonds are approximately 0.25 Å longer than their Mn^{IV} counterparts. Once again, the structural data serve to highlight the rigidity of the tacn ligand, which not only leads to a less flexible structure but may also predispose the Mn^{III} site towards a low-spin configuration.

Both the composition of the molecular orbitals given in Table 3 and their relative energies, shown in Figure 2, are consistent with the presence of distinct Mn^{III} and Mn^{IV} sites in the mixed-valence dimer. Table 3 lists the compositions for both the spin-up and spin-down orbitals since, unlike the IV/IV and III/III systems, the compositions of the spin-down orbitals do not mirror those of the spin-up orbitals. However, it is clear from Figure 2 that the majority spin 26a′, 27a′, and 17a″ t_{2g} orbitals on either center are very similar to those for the symmetric IV/IV and III/III dimers in terms of both composition and relative energies. The additional unpaired electron is found to occupy the 28a′↑ orbital, and thus, the resulting BS configuration corresponds to $(26a'\uparrow)^1(26a'\downarrow)^1(27a'\uparrow)^1(27a'\downarrow)^1(17a''\uparrow)^1(17a''\downarrow)^1(28a'\uparrow)^1$. The 28a′↑ HOMO is found to be comprised of a mixture of 44% majority spin d_{z^2} on Mn^{III}, 24% minority spin $d_{x^2-y^2}$ on Mn^{IV}, and 14% bridging carboxylate character, the bridging oxo contribution to this orbital being negligible. The high-spin nature of the Mn^{III} ion is confirmed from its calculated net spin density of +3.57 and also by the fact that the largest contribution to the HOMO is the majority spin d_{z^2} orbital on Mn^{III}. Based on the Mn^{III}:Mn^{IV} ratio of approximately 44:24, the 28a′ HOMO is significantly delocalized across both metal centers. This result is in stark contrast with the III/III dimer, where the occupied 28a′ HOMO is essentially localized on opposite Mn centers, but parallels the strong delocalization (27:48) found for the 28a′ LUMO in the IV/IV dimer.

From Table 3 and the relevant contour plot in Figure 3, the delocalization of the 28a′↑ level in the mixed-valence dimer involves the crossed exchange $J_{x^2-y^2/z^2}$ pathway, where the charge from the majority spin d_{z^2} orbital on Mn^{III} is transferred to the minority spin $d_{x^2-y^2}$ orbital on Mn^{IV}. As discussed previously, in the case of the IV/IV dimer, this pathway becomes favorable when the combined effect of a small axial ligand field on Mn^{III} and lower spin-polarization splitting on Mn^{IV} places the majority spin d_{z^2} orbital on Mn^{III} in close proximity to the minority spin $d_{x^2-y^2}$ orbital on Mn^{IV}. In our earlier study of the mixed-valence dimer $[Mn(\mu\text{-}O)_2(NH_3)_8]^{3+}$, we found the same crossed exchange pathway was responsible for the delocalization of the unpaired electron; but in this case, the delocalization over both Mn centers was significantly lower, approximately 4:1. In the DFT study of $[Mn(\mu\text{-}O)_2(OAc)(tacn)_2]^{2+}$, completed by Noodleman and co-workers,[29] the equivalent HOMO was almost completely delocalized over both Mn centers. However, in this system, the extensive delocalization can be attributed to the fixed structure used in their calculation which, as noted earlier, involved equivalent Mn sites due to crystallographic disorder. As a consequence, the Mn^{III} ion is low spin and the majority spin d_{z^2} orbital is not stabilized by a Jahn−Teller distortion. Fortuitously, this resulted in a close match in energy of the majority spin d_{z^2} and minority spin $d_{x^2-y^2}$ orbitals on opposite Mn centers and, consequently, substantial delocalization of the odd electron. In contrast, the optimized structure of $[Mn_2(\mu\text{-}O)_2(O_2CH)(NH_3)_6]^{2+}$ contains high-spin Mn^{III}, and the elongation of the Mn−O_c and Mn−N_{ax} bonds due to the Jahn−Teller effect stabilizes the d_{z^2} orbital on Mn^{III}. This in turn leads to an increased energy difference between the majority spin d_{z^2} orbital on Mn^{III} and the minority spin $d_{x^2-y^2}$ orbital on Mn^{IV} and thus reduces the effectiveness of the crossed exchange delocalization mechanism. The partial delocalization of the unpaired electron via the crossed exchange $J_{x^2-y^2/z^2}$ pathway found in this study nicely rationalizes the structure of the mixed-valence $[Mn_2(\mu\text{-}O)_2(O_2CH)(NH_3)_6]^{2+}$ dimer. The reduced elongation of the axial Mn^{III}−O_c and Mn^{III}−N_{ax} bonds relative to the III/III dimer arises from the loss of electron density in the majority spin d_{z^2} orbital due to the delocalization onto Mn^{IV}. The fact that the extra electron density on Mn^{IV} is not reflected in any structural differences compared to the IV/IV dimer can be accounted for on the basis that the additional electron density enters the minority spin $d_{x^2-y^2}$ orbital on Mn^{IV}, which is nonbonding with respect to the N and O_c donors.

Comparisons Between Oxidation States in $[Mn_2(\mu\text{-}O)_2(O_2CH)(NH_3)_6]^{n+}$. As the $[Mn_2(\mu\text{-}O)_2(O_2CH)(NH_3)_6]^{3+}$ dimer is progressively reduced, the Mn−Mn distance changes from 2.738 Å in the IV/IV state to 2.667 and 2.595 Å in the III/IV and III/III states, respectively. The changes in the Mn−Mn distance are mirrored by the Mn−O−Mn angle, which decreases from 97° for the IV/IV oxidation state to 90° for the III/III state. In addition, the tilt of the Mn_2O_2 core progressively increases from 21° in the IV/IV dimer to 31° in the III/III species. The most drastic differences in structure arising from change in oxidation state is in relation to the axial Mn−O_c and Mn−N_{ax} bonds, due to the Jahn Teller distortion of the high-spin Mn^{III} ions. In the III/III dimer, the Mn−O_c and Mn−N_{ax} distances of 2.32 and 2.45 Å, respectively, are considerably longer than the distances of 1.99 and 2.11 Å in the IV/IV dimer. In the mixed-valence dimer, the partial delocalization of the unpaired electron results in intermediate elongation of the Mn^{III}−O_c and Mn^{III}−N_{ax} bonds relative to the III/III dimer, but these bonds are still significantly longer than their counterparts on the Mn^{IV} site.

The structural changes noted above are important in understanding the differences in magnetic coupling in the three oxidation states of the $[Mn_2(\mu\text{-}O)_2(O_2CH)(NH_3)_6]^{n+}$ system. The analysis of the electronic structure of the IV/IV, III/IV, and III/III dimers has shown that the most important exchange interactions between the Mn centers involve the symmetric $J_{xz/xz}$ and $J_{yz/yz}$ pathways, which are mediated through overlap of the Mn d_{xz} and d_{yz} orbitals with the out-of-plane pπ orbitals on the oxo bridges (see Figure 4). In the case of the mixed-valence III/IV dimer, the crossed exchange $J_{x^2-y^2/z^2}$ pathway is also important in accounting for the delocalization of the unpaired electron. Since the d_{xz} and d_{yz} orbitals on each Mn center are singly occupied in all three oxidation states, the $J_{xz/xz}$ and $J_{yz/yz}$ pathways will always make antiferromagnetic contributions to the overall exchange coupling constant. In contrast, the $J_{x^2-y^2/z^2}$ pathway in both the IV/IV and III/IV dimers involves overlap of a half filled orbital on one metal with a vacant orbital on the other and, as shown by Girerd and co-workers,[53−55] this type of exchange pathway is ferromagnetic in origin. However, for the III/III dimer, both the $d_{x^2-y^2}$ and d_{z^2} orbitals are half filled with the result that the crossed exchange $J_{x^2-y^2/z^2}$ pathway is converted from a ferromagnetic interaction to an antiferromagnetic one.

In our earlier study of the di-μ-oxo bridged system $[Mn_2(\mu\text{-}O)_2(NH_3)_8]^{n+}$, containing a planar Mn_2O_2 core, we showed that elongation of the dimer along the metal−metal axis, such that the O−Mn−O angle is reduced from 90°, resulted in better overlap of the d_{yz} orbitals on each Mn center with the out-of-plane oxo pπ orbitals. Consequently, in the IV/IV dimer, where the Mn−Mn separation is greater and thus the O−Mn−O angle more acute, the improved overlap of the d_{yz} orbitals with the bridging oxo ligands leads to a more efficient $J_{yz/yz}$ pathway and accordingly, a larger antiferromagnetic exchange coupling constant. In the present system $[Mn_2(\mu\text{-}O)_2(O_2CH)(NH_3)_6]^{n+}$, the nonplanar Mn_2O_2 core will reduce the overlap of both the d_{xz} and d_{yz} metal orbitals with the out-of-plane oxo pπ orbitals, and therefore, for a given Mn−Mn distance, the $J_{xz/xz}$ and $J_{yz/yz}$ pathways will be less efficient than in the planar di-μ-oxo bridged system. This is reflected in the calculated exchange coupling constants given in Table 5 for the IV/IV oxidation states where the value of $-J = 274\ cm^{-1}$ for the planar $[Mn_2(\mu\text{-}O)_2(NH_3)_8]^{4+}$ dimer is approximately twice as large as the value of $-J = 129\ cm^{-1}$ for $[Mn_2(\mu\text{-}O)_2(O_2CH)(NH_3)_6]^{3+}$. However, the nonplanarity of the $[Mn_2(\mu\text{-}O)_2(O_2CH)(NH_3)_6]^{n+}$ system does not affect the validity of the above geometric arguments relating to the overlap of the metal d_{yz} orbital with the out-of-plane oxo pπ orbitals. Accordingly, we anticipate that the shorter Mn−Mn distance in the III/III dimer, due to the more compressed geometry of the Mn_2O_2 core, will result in weaker antiferromagnetic coupling compared to the IV/IV dimer. However, this prediction is not borne out in the calculated exchange coupling constants given in Table 5 where the value of $-J = 176\ cm^{-1}$ for the IIII/III dimer is over 45 cm^{-1} larger than the value for the IV/IV dimer. To rationalize this result, it is necessary to examine the geometry dependence of the exchange pathways. Accordingly, we have plotted the energies of the magnetic orbitals in the S_{max} state for the III/III and IV/IV dimers in Figure 5 , as a function of the Mn−Mn separation.

(53) Wieghardt, K.; Bossek, U.; Nuber, B.; Weiss, J.; Bonvoisin, J.; Corbella, M.; Vitols, S. E.; Girerd, J. J. *J. Am. Chem. Soc.* **1988**, *110*, 7398.
(54) Blondin, G.; Girerd, J.-J. *Chem. Rev.* **1990**, *90*, 1359.
(55) Hotzelmann, R.; Wieghardt, K.; Florke, U.; Haupt, H.-J.; Weatherburn, D. C.; Bonvoisin, J.; Blondin, G.; Girerd, J.-J. *J. Am. Chem. Soc.* **1992**, *114*, 1681.

Table 4. (A) Mulliken Decomposition of the Essentially Mn Based Molecular Orbitals into Contributions from the Mn and Bridging Ligands for the IV/IV and III/III Dimers of $[Mn_2(\mu\text{-}O)(HCO_2)_2(NH_3)_6]^{n+}$. Atomic Orbital Contributions to Molecular Orbitals Are Listed in Order of Weighting. Only Spin-up Orbitals Are Listed. (B) Mulliken Decomposition of the Essentially Mn Based Molecular Orbitals into Contributions from the Mn and Bridging Ligands for the Two Possible Ground States of the III/IV Dimer $[Mn_2(\mu\text{-}O)(HCO_2)_2(NH_3)_6]^{3+}$ Involving High-Spin and Low-Spin Mn^{III}. Atomic Orbital Contributions to Molecular Orbitals are Listed in Order of Weighing

A

MO	energy/eV	occ	Mn_1	Mn_2	O	O_c	N
			$[Mn_2(\mu\text{-}O)(HCO_2)_2(NH_3)_6]^{4+}$				
26a′↑	−22.771	2	39 $d_{x^2-y^2}$	4	0	49	2
28a′↑	−22.077	2	26 d_{yz}	7 d_{yz}, d_{z^2}	24	26	12
21a″↑	−21.933	2	24 d_{xz}	10 d_{xz}	28	26	6
29a′↑	−20.069	0	1	87 $d_{x^2-y^2}$	0	7	0
30a′↑	−19.924	0	14 d_{z^2}	64 d_{yz}	6	2	10
22a″↑	−19.693	0	36 d_{xy}	24 d_{xz}	5	10	18
23a″↑	−19.632	0	16 d_{xy}	54 d_{xz}	12	9	5
31a′↑	−18.994	0	35 d_{z^2}	25 d_{yz}, d_{z^2}	17	8	12
24a″↑	−18.497	0	1	64 d_{xy}	0	14	15
32a′↑	−17.784	0	6	57 d_{z^2}	15	5	14
			$[Mn_2(\mu\text{-}O)(HCO_2)_2(NH_3)_6]^{2+}$				
27a′↑	−13.354	2	60 $d_{x^2-y^2}$	2	2	29	2
28a′↑	−13.133	2	44 d_{yz}	6 d_{z^2}, d_{yz}	25	14	7
21a″↑	−12.820	2	36 d_{xz}	10 d_{xz}	32	15	3
22a″↑	−11.462	2	54 d_{xy}	1	0	22	15
29a′↑	−10.870	0	43 d_{z^2}	26 d_{yz}	6	7	12
30a′↑	−9.991	0	0	91 $d_{x^2-y^2}$	0	3	0
23a″↑	−9.850	0	1	82 d_{xz}	13	0	0
31a′↑	−9.646	0	12 d_{z^2}	65 d_{yz}	15	3	2
24a″↑	−8.643	0	0	81 d_{xy}	0	8	6
32a′↑	−8.768	0	2	69 d_{z^2}	11	4	9

B

MO	energy/eV	occ	Mn_1	Mn_2	O	O_c	N
			$[Mn_2(\mu\text{-}O)(HCO_2)_2(NH_3)_6]^{3+}$ (High-Spin Mn^{III})				
27a′↓	−18.030	1	3	30 $d_{x^2-y^2}$	1	54	6
27a′↑	−17.868	1	69 $d_{x^2-y^2}$	3	0	22	1
28a′↑	−17.566	1	43 d_{yz}	11 d_{yz}, d_{z^2}	25	9	9
28a′↓	−17.519	1	5 d_{z^2}, d_{yz}	25 d_{yz}	21	34	9
21a″↑	−17.469	1	35 d_{xz}	16 d_{xz}	27	13	3
21a″↓	−17.240	1	5 d_{xz}	25 d_{xz}	26	33	5
22a″↑	−15.709	1	51 d_{xy}	1	0	18	22
29a′↑	−15.635	0	10 d_{z^2}	52 $d_{x^2-y^2}$, d_{yz}	2	5	5
30a′↑	−15.584	0	13 d_{z^2}	32 $d_{x^2-y^2}$, d_{yz}	3	6	7
22a″↓	−15.272	0	1	50 d_{xy}	0	21	17
23a″↑	−15.085	0	2	71 d_{xz}	21	2	1
29a′↓	−15.019	0	30 d_{yz}	39 d_{z^2}	6	6	14
31a′↑	−14.609	0	30 d_{z^2}	30 d_{yz}	20	8	8
30a′↓	−14.378	0	90 $d_{x^2-y^2}$	1	0	3	0
23a″↓	−14.336	0	86 d_{xz}	1	10	1	0
24a″↑	−14.166	0	0	67 d_{xy}	0	15	12
31a′↓	−14.070	0	66 d_{yz}	13 d_{z^2}	14	3	3
32a′↑	−13.426	0	5 d_{z^2}	60 d_{z^2}	15	5	12
32a′↓	−13.097	0	66 d_{z^2}	4 d_{z^2}	11	4	11
24a″↓	−12.968	0	80 d_{xy}	0	0	7	9
			$[Mn_2(\mu\text{-}O)(HCO_2)_2(NH_3)_6]^{3+}$ (Low-Spin Mn^{III})				
26a′↑	−18.432	1	45 $d_{x^2-y^2}$	2	0	42	4
27a′↓	−17.899	1	3	62 $d_{x^2-y^2}$	2	25	3
28a′↑	−17.547	1	39 d_{yz}	6 d_{yz}, d_{z^2}	29	12	11
21a″↑	−17.340	1	35 d_{xz}	11 d_{xz}	32	14	3
21a″↓	−16.907	1	11d_{xz}	49 d_{xz}	30	8	2
28a′↓	−16.706	1	6 d_{z^2}, d_{yz}	64 d_{yz}	18	4	5
29a′↑	−15.580	1	29 d_{z^2}	45 d_{yz}	3	4	14
22a″↑	−15.386	0	54 d_{xy}	1	0	19	19
29a′↓	−15.241	0	88 $d_{x^2-y^2}$	1	0	5	0
30a′↑	−15.218	0	0	88 $d_{x^2-y^2}$	0	5	0
30a′↓	−14.938	0	74 d_{yz}	12 d_{z^2}	4	2	5
22a″↓	−14.788	0	6	56 d_{xy}	1	14	17
23a″↓	−14.617	0	76 d_{xz}	4 d_{xy}	13	3	1
23a″↑	−14.589	0	2	77 d_{xz}	18	1	1
31a′↑	−14.372	0	24 d_{z^2}	40 d_{yz}	22	4	6
24a″↓	−13.862	0	69 d_{xy}	1	0	12	12
24a″↑	−13.808	0	0	69 d_{xy}	0	12	13
31a′↓	−13.732	0	22 d_{yz}, d_{z^2}	42 d_{z^2}	16	6	16
32a′↓	−12.857	0	61 d_{z^2}	7 d_{z^2}	14	3	10
32a′↑	−12.792	0	2 d_{z^2}	65 d_{z^2}	13	4	10

Table 5. Experimental and Calculated Magnetic Data and Net Spin Densities (S) on the Mn Ions

oxid'n state	spin state	$-J/cm^{-1}$ expt	$-J/cm^{-1}$ calc	B/cm^{-1} calc	S(Mn)
		$[Mn_2(\mu\text{-}O)_2(HCO_2)(NH_3)_6]^{n+}$			
IV−IV	3	67−124	129		±2.75
III−IV	7/2	114−220	268	135	+3.57
					−2.41
III−III	4		176		±3.61
		$[Mn_2(\mu\text{-}O)(HCO_2)_2(NH_3)_6]^{n+}$			
IV−IV	3		180		±2.83
III−IV	7/2		154	406	+3.77
		−40			−2.70
	5/2		−11	401	+3.35
					−2.31
III−III	4	−9−9	25		±3.75

The energetic separation of the symmetric (+) and antisymmetric (−) combinations of metal based orbitals in the S_{max} state of a dimer is known to reflect the contribution of the exchange pathway involving these orbitals to the overall ground-state magnetic coupling.[58] These plots reveal that the decrease in the $J_{yz/yz}$ pathway for the III/III dimer relative to IV/IV is effectively compensated by the increase in $J_{xz/xz}$. In addition, as noted earlier, the crossed exchange $J_{x^2-y^2/z^2}$ pathway converts from a ferromagnetic interaction in the IV/IV dimer to an antiferromagnetic one in the III/III oxidation state. Given the significant mixing of this pathway with $J_{x^2-y^2/x^2-y^2}$, the latter will be largely minimized if not ferromagnetic in origin for the IV/IV dimer. Furthermore, in the III/III dimer there is also a small antiferromagnetic contribution from the symmetric J_{z^2/z^2} pathway. Taking all these interactions into consideration would tend to indicate that the ground-state magnetic coupling in the III/III dimer should be greater than that occurring in the IV/IV oxidation state, consistent with the calculated J values. The plots also show that for Mn−Mn distances between 2.6 and 2.8 Å, there is little variation in the contributions of the $J_{xz/xz}$ and $J_{yz/yz}$ pathways from both the III/III and IV/IV dimers. In contrast, while the contribution of the symmetric $J_{x^2-y^2/x^2-y^2}$ pathway is significantly smaller, it exhibits dramatic changes in both dimers over the same range of Mn−Mn separations.

For the mixed-valence III/IV dimer, calculated values of $-J = 268\ cm^{-1}$ and $B = 135\ cm^{-1}$ are obtained using eqs 5 and 6. Although the rather small value of B is comparable to the value of $B = 143\ cm^{-1}$ calculated for the planar di-μ-oxo III/IV complex, it is seemingly at odds with the significant delocalization of the unpaired electron in the 28a′ HOMO. However, B is determined from the energies of the delocalized high-spin states, $E(S_{max})_g$ and $E(S_{max})_u$, where the crossed exchange $J_{x^2-y^2/z^2}$ pathway is eliminated. The above value of B therefore reflects only the symmetric J_{z^2/z^2} pathway rather than $J_{x^2-y^2/z^2}$ which, on the basis of the composition of the 28a′ HOMO, is primarily responsible for the electron delocalization.

Finally, before leaving this section, it is worth commenting on why the crossed exchange $J_{x^2-y^2/z^2}$ pathway is more efficient in the nonplanar III/IV dimer $[Mn_2(\mu\text{-}O)_2(O_2CH)(NH_3)_6]^{2+}$ than in the planar $[Mn_2(\mu\text{-}O)_2(NH_3)_8]^{3+}$ analogue. In the former system, the introduction of the carboxylate bridge and consequent tilting of the Mn_2O_2 core causes changes in both the ligand-field and spin-polarization splittings, such that the majority spin e_g orbitals on the Mn^{III} center lie energetically

(56) Weihe, H.; Gudel, H. U. *J. Am. Chem. Soc.* **1998**, *120*, 2870.
(57) Wu, F.-J.; Kurtz, D. M.; Hagen, K. S.; Nyman, P. D.; Debrunner, P. G.; Vankai, V. A. *Inorg. Chem.* **1990**, *29*, 5174.
(58) Hay, P. J.; Thibeault, J. C.; Hoffmann, R. *J. Am. Chem. Soc.* **1975**, *97*, 4884.

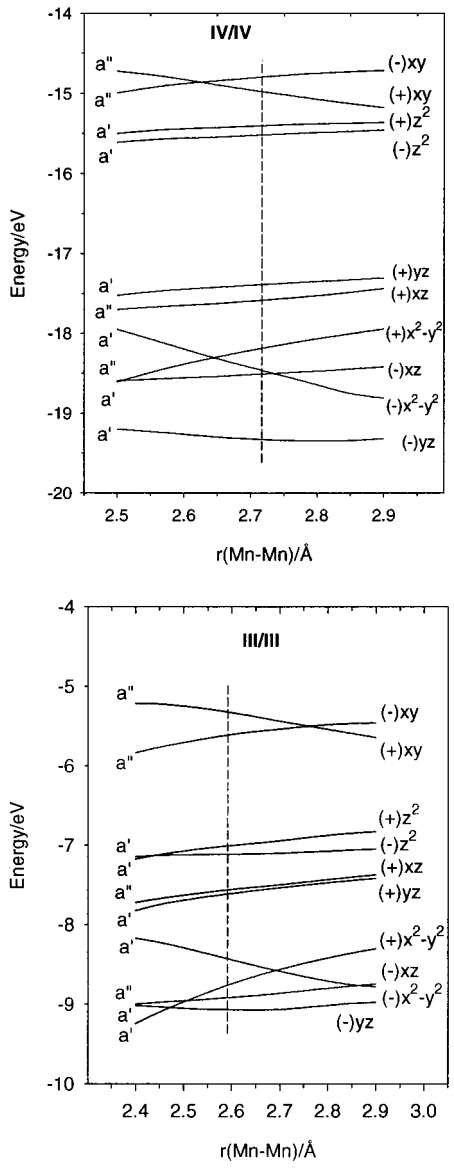

Figure 5. Energies of the symmetric (+) and antisymmetric (−) combinations of d orbitals in the high-spin state as a function of the Mn−Mn separation for (a) $[Mn_2(\mu\text{-}O)_2(HCO_2)(NH_3)_6]^{3+}$ and (b) $[Mn_2(\mu\text{-}O)_2(HCO_2)(NH_3)_6]^{1+}$. Vertical lines correspond to calculated Mn−Mn distances in BS state.

closer to the minority spin t_{2g} orbitals of Mn^{IV}. The reduced energy gap facilitates mixing between orbitals of the same symmetry and, in particular, enhances delocalization via the $J_{x^2-y^2/z^2}$ pathway. One consequence of electron delocalization via the crossed $J_{x^2-y^2/z^2}$ pathway is that it partially converts the Mn^{IV} and Mn^{III} ions into low-spin Mn^{III} and Mn^{IV}, respectively. This is reflected in the lower net spin density of 2.41 on Mn^{IV} in the mixed-valence complex compared to 2.75 in the IV/IV dimer. Accordingly, the magnetic coupling in the III/IV dimer can be considered to arise from two interacting spin ladders, one the result of coupling between Mn^{IV} ($S = 3/2$) and high-spin Mn^{III} ($S = 2$), the other between Mn^{IV} ($S = 3/2$) and low-spin Mn^{III} ($S = 1$). This description differs from that of Noodleman and co-workers in their study of $[Mn(\mu\text{-}O)_2(OAc)(tacn)_2]^{2+}$, where the Mn^{III} ion is formally low-spin not high-spin, and the spin ladders based on low-spin Mn^{III} ($S = 1$) and high-spin Mn^{III} ($S = 2$) are energetically very close. In the case of $[Mn_2(\mu\text{-}O)_2(O_2CH)(NH_3)_6]^{2+}$ however, the nearest excited BS state where the Mn^{III} is low-spin is calculated to lie over 0.5 eV higher in energy. The differences between the two systems can be directly attributed to the greater ligand field strength and rigidity of the tacn donor relative to NH_3, which reduces the Jahn−Teller axial distortion, thus favoring a low-spin Mn^{III} geometry.

$[Mn_2(\mu\text{-}O)(O_2CH)_2(NH_3)_6]^{n+}$. IV/IV Dimer. The optimized structural parameters for $[Mn_2(\mu\text{-}O)(O_2CH)_2(NH_3)_6]^{4+}$ are given in Table 2. Unfortunately, no complexes containing a $[Mn_2(\mu\text{-}O)(O_2CR)_2]^{n+}$ core in the IV/IV oxidation state have been structurally characterized. However, relative to the calculated geometry of the di-μ-oxo, μ-carboxylato dimer in the IV/IV oxidation state, there are a number of significant changes. Most notably, the dimer has undergone a dramatic elongation along the metal−metal axis, with the calculated Mn−Mn distance of 3.304 Å and the Mn−O−Mn angle of 133° corresponding to increases of 0.57 Å and 36°, respectively. All other structural parameters involving Mn−O, Mn−O_c, and Mn−N bond lengths are similar, with differences within 0.05 Å.

Analogous to the di-μ-oxo, μ-carboxylato dimers, a local reference frame for the Mn centers is used to simplify the discussion of the electronic structure. As shown in Figure 1, the local *z*-axis for each Mn ion is defined to be parallel to the Mn−O bond axis, and the *y*-axis is defined such that the Mn−Mn vector is in the *yz* plane. With this definition of quantisation axes, the composition and transformation of the t_{2g} (d_{xz}, d_{yz}, and $d_{x^2-y^2}$) and e_g (d_{z^2} and d_{xy}) orbitals in C_s symmetry remains unchanged from those of $[Mn_2(\mu\text{-}O)_2(O_2CH)(NH_3)_6]^{n+}$. Since the oxo ligand is a stronger donor than carboxylate, the ligand field is equivalent to a tetragonal compression (alternatively, equatorial elongation), with the tetragonal axis along the Mn−O bond, which splits the degeneracy of the e_g orbitals such that the d_{z^2} orbital lies to higher energy than the d_{xy}. The effect on the t_{2g} orbitals is generally less pronounced, but the $d_{x^2-y^2}$ orbital should lie at a lower energy than d_{xz} and d_{yz}.

The energies of the metal based orbitals and their compositions are shown in Figure 6 and Table 4a, respectively. As far as the majority spin t_{2g} and minority spin e_g orbitals are concerned, the calculated BS state, corresponding to the configuration $(26a'\uparrow)^1(26a'\downarrow)^1(28a'\uparrow)^1(28a'\downarrow)^1(21a''\uparrow)^1(21a''\downarrow)^1$, reflects the above description of the low-symmetry splitting of the Mn centers. The majority spin t_{2g} orbitals 26a′ ($d_{x^2-y^2}$), 28a′ (d_{yz}) and 21a″ (d_{xz}) are all close in energy, but the 26a′ level is stabilized by over 0.5 eV relative to the other two. The 27a′ level is not shown in Figure 6 as it is essentially a ligand-based orbital, considering its composition of approximately 55% O_c and 22% N. The proximity of this and other ligand-based orbitals to the majority spin t_{2g} manifold results in the latter being highly covalent, accounting for the relatively low metal contributions to these levels in Table 4a. As expected, the tetragonal distortion results in a 0.7 eV splitting of the minority spin e_g orbitals, 24a″ (d_{xy}) and 32a′ (d_{z^2}), with the 24a″ level lying at lowest energy, consistent with a tetragonally compressed Mn^{IV} geometry. The description of the minority spin t_{2g} and majority spin e_g orbitals however, is not so straightforward. The combined effect of the ligand field and spin polarization splittings result in a situation where these orbitals are very close in energy, and because of the low C_s symmetry, there is substantial mixing between the two sets as is evident from the orbital compositions in Table 4a and the relevant contour plots in Figure 7. In particular, the 22a″ and 31a″ levels are significantly delocalized with Mn_1:Mn_2 ratios of 36:24 and 35:25, respectively.

Of the occupied t_{2g} orbitals, only the d_{xz} and d_{yz} orbitals are capable of interacting with the pπ orbitals of the single oxo bridge, as can be seen from the schematic representations of

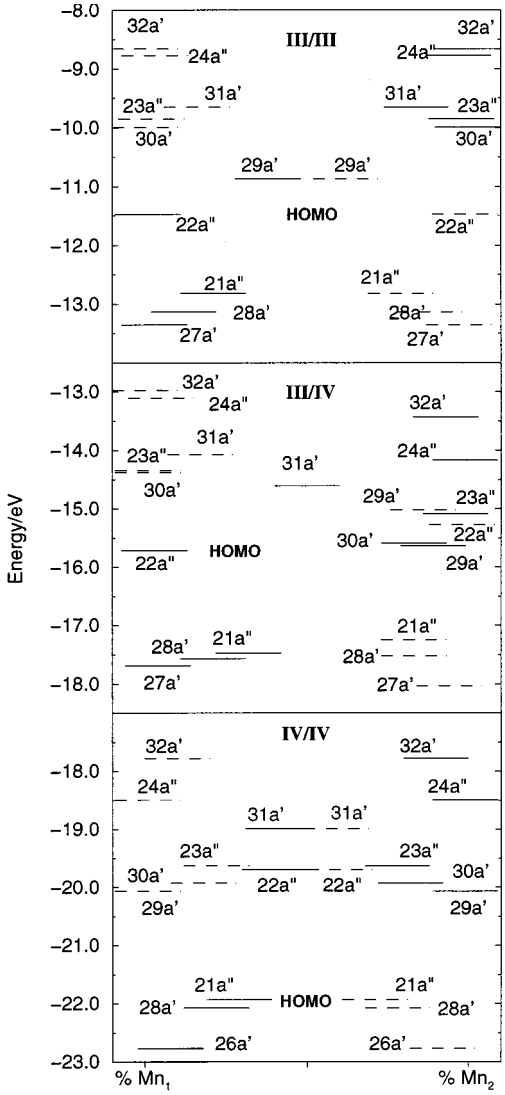

Figure 6. Energies and delocalization of the metal-based orbitals obtained from broken-symmetry calculations for $[Mn_2(\mu\text{-}O)(HCO_2)_2(NH_3)_6]^{n+}$ in the $Mn^{IV}Mn^{IV}$, $Mn^{III}Mn^{IV}$, and $Mn^{III}Mn^{III}$ oxidation states.

these exchange pathways in Figure 8. The bent Mn_2O structure, corresponding to a Mn−O−Mn angle of 133°, disrupts the overlap of the d_{yz} orbital with the in-plane oxo pπ orbital. In contrast, overlap of the Mn d_{xz} and out-of-plane oxo pπ orbital is not affected by changes in the Mn−O−Mn angle. On the basis of these geometric considerations, the $J_{xz/xz}$ exchange pathway is expected to be the most efficient pathway for magnetic exchange between the two Mn ions. This simple analysis is borne out in the compositions of the 28a′ (d_{yz}) and 21a″ (d_{xz}) orbitals, which exhibit Mn_1:Mn_2 delocalization ratios of 26:7 and 24:10, respectively. The large contribution of the oxo donor to both of these orbitals confirms that superexchange through the oxo bridge is responsible for the delocalization. From the orbital compositions in Table 4a, the crossed-exchange J_{yz/z^2} pathway also makes a small contribution to the 28a′ level. Since the d_{z^2} orbital is unoccupied, this pathway is ferromagnetic. The contribution of the carboxylate oxygens to the 28a′ and 21a″ levels is comparable to that of the oxo bridge, approximately 26%. However, since the contour plots of these orbitals in Figure 7 show that most of this contribution is centered on only one Mn site, it can be concluded that the carboxylate bridge is not important to the $J_{xz/xz}$ and $J_{yz/yz}$ pathways. From Table 4a, the extent of delocalization for the 26a′ ($d_{x^2-y^2}$) orbital is much smaller than that for 28a′ and 21a″. The contribution of the carboxylate oxygens to this level however is considerably larger, approximately 49%, with negligible oxo character. A decomposition of the O_c contributions reveals that the carboxylate oxygens on both Mn centers contribute significantly to the 26a′ orbital, and therefore, the carboxylate bridge is mainly responsible for mediating the magnetic exchange, albeit weak, via the $J_{x^2-y^2/x^2-y^2}$ pathway. From the orbital decompositions in Table 4a, it is apparent that the significant delocalization of the 22a″ and 31a′ levels arises from two different crossed-exchange pathways, namely $J_{xy/xz}$ for the 22a″ level and J_{yz/z^2} for 31a′. Schematics of these crossed-exchange pathways are shown in Figure 8. In the case of J_{yz/z^2}, the in-plane oxo pπ orbital is responsible for mediating the superexchange, whereas for $J_{xy/xz}$, the out-of-plane oxo pπ orbital is involved.

III/III Dimer. The calculated geometry of $[Mn_2(\mu\text{-}O)(O_2CH)_2(NH_3)_6]^{2+}$ given in Table 2 compares well with published crystal data given in Table 1. The calculated Mn−Mn distance of 3.179 Å, although toward the high end, is well within the range of observed Mn−Mn distances. The Mn−O distance also compares favorably, but the Mn−N_{ax} and Mn−N_{eq} distances are slightly longer than the reported values. Once again, this deviation can be mostly attributed to the differences between the unsaturated or cyclically constrained N donors present in the experimental structures and the simple amine donors used in the model structures. Compared to the calculated structure of the IV/IV dimer, a reduction in the Mn−Mn distance of 0.12 Å and an increase in the Mn−O−Mn angle of 9° have occurred. In the calculated structure, the Mn−N_{eq} distance is found to be 0.15 Å longer than Mn−N_{ax}, and significant increases in both the Mn−N_{eq} and Mn−O_c bond distances of approximately 0.18 and 0.15 Å, respectively, are observed relative to the IV/IV dimer. These structural differences can be attributed to the compressed axial geometry around each Mn^{III} ion due to the Jahn−Teller distortion.

The relative energies and compositions of the majority spin t_{2g} orbitals 27a′, 28a′, and 21a″ are essentially the same as those described for the IV/IV dimer. On reduction from the IV/IV to the III/III oxidation state, the additional electrons occupy the 22a″ HOMO, corresponding to the majority spin d_{xy} orbitals on each Mn center. The Mn^{III} centers are therefore high-spin, consistent with the calculated net spin density of ±3.75 on each metal ion. The occupation of the d_{xy} orbital in the high-spin structure implies a tetragonally compressed geometry where the d_{z^2} orbital is destabilized relative to d_{xy}. This energetic ordering can be intuitively understood on the basis that the oxo ligand is a stronger donor than carboxylate, and therefore, the axial ligand field is greater than the equatorial field. Occupation of the metal−ligand antibonding d_{xy} orbital leads to longer Mn^{III}−N_{eq} bonds relative to Mn^{III}−N_{ax}, and longer Mn−O_c and Mn−N_{eq} bonds compared to the IV/IV structure.

From Table 4a and the relevant contour plots in Figure 7, the main magnetic interactions between the two Mn ions occur via the 28a′ and 21a″ levels which exhibit Mn_1:Mn_2 delocalization ratios of 44:6 and 36:10, respectively. The 28a′ level involves the symmetric $J_{xz/xz}$ exchange pathway and represents the major antiferromagnetic pathway in this system. The 28a′ orbital on the other hand, primarily involves the crossed J_{yz/z^2} exchange pathway which is ferromagnetic in origin due to the d_{z^2} orbital being vacant. The opposite sign of $J_{xz/xz}$ and J_{yz/z^2} implies that these two pathways will cancel each other to some extent, and therefore, the overall exchange coupling will be much smaller than in the IV/IV dimer where both the 28a′ and 21a″ levels involve antiferromagnetic pathways.

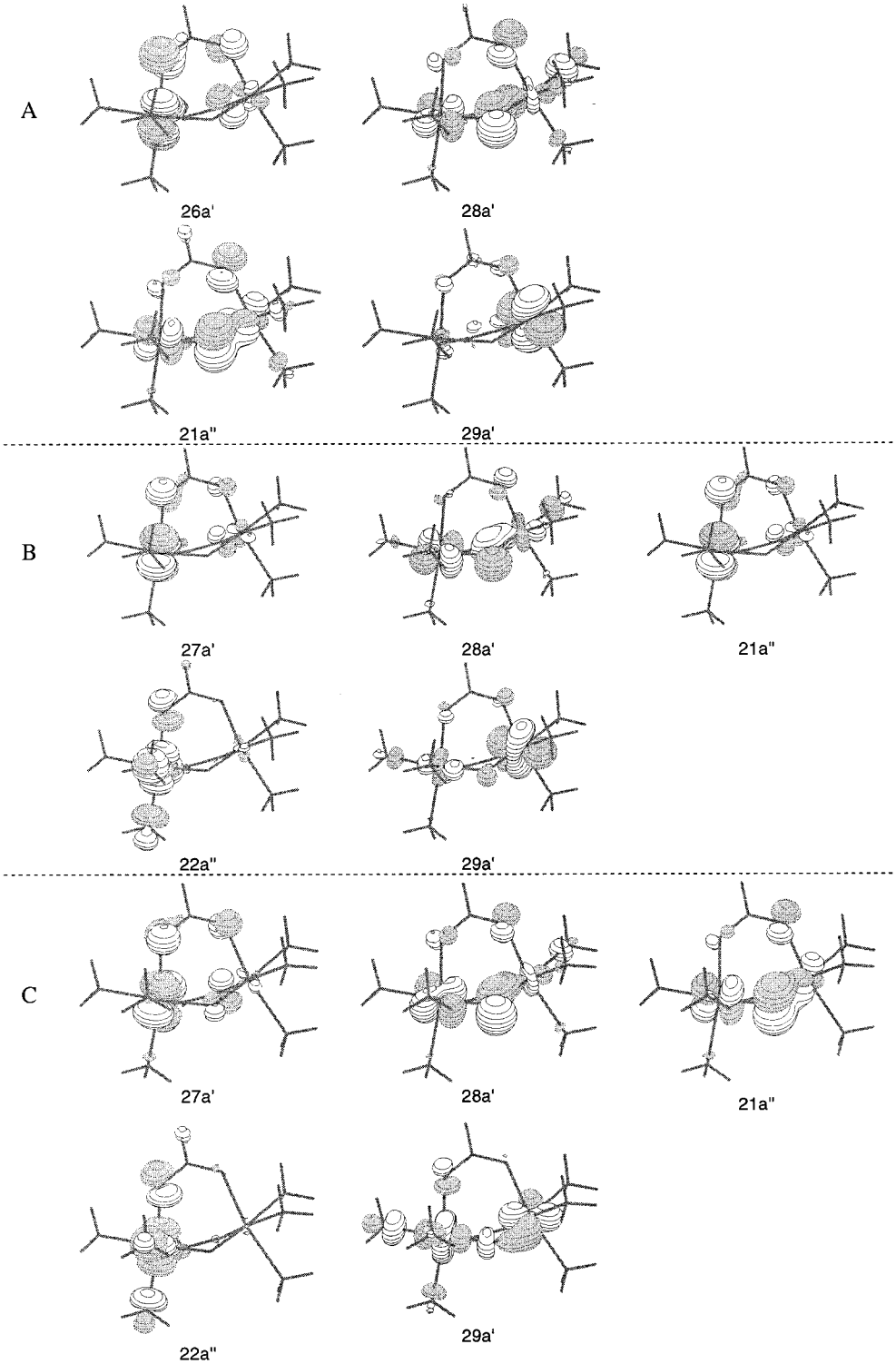

Figure 7. Surface plots of the Mn based occupied MOs and LUMO obtained from broken-symmetry calculations on (a) $[Mn_2(\mu\text{-}O)(HCO_2)_2(NH_3)_6]^{4+}$, (b) $[Mn_2(\mu\text{-}O)(HCO_2)_2(NH_3)_6]^{3+}$, and (c) $[Mn_2(\mu\text{-}O)(HCO_2)_2(NH_3)_6]^{2+}$.

One other significant difference between the III/III and IV/IV dimers concerns the lack of delocalization of the 22a″ HOMO in the former. As noted earlier, in the IV/IV dimer this level is substantially delocalized (36:24) due to the close approach of the 22a″ and 23a″ orbitals (see Figure 6), which gives rise to strong mixing of the majority spin d_{xy} and minority spin d_{xz} orbitals on opposite Mn centers. The closeness of these two levels in the IV/IV dimer can be linked to the fact that the destabilization of the majority spin d_{xy} orbital on one Mn ion, due to the ligand field splitting, is comparable to the destabilization of the minority spin d_{xz} orbital on the other as a result of the spin polarization splitting. In the III/III dimer however, the same processes on each Mn center act in the opposite sense. The axially compressed geometry of the Mn^{III} ions produces a smaller equatorial ligand field, thus stabilizing the majority spin d_{xy} orbital over d_{z^2}. In contrast, the higher spin-polarization splitting of the Mn^{III} ions results in a greater destabilization of the minority spin d_{xz} orbital relative to the IV/IV dimer. The combined effect produces a large energetic separation (over 1.5 eV) of these two orbitals in the III/III dimer and thus little

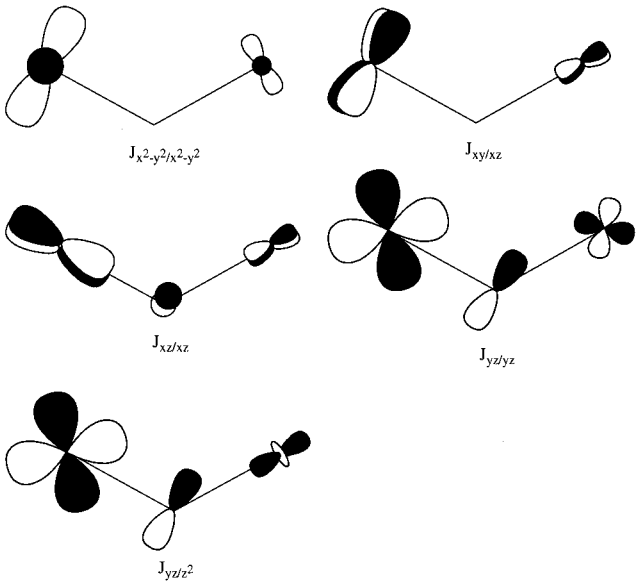

Figure 8. Schematic representation of the main exchange pathways in $[Mn_2(\mu\text{-}O)(HCO_2)_2(NH_3)_6]^{n+}$ complexes.

mixing between them. From Figure 6 and Table 4a, the delocalization of the 29a′ LUMO in the III/III dimer is also quite marked (43:26) and involves mixing of the majority spin d_{z^2} orbital on one Mn center with the minority spin d_{yz} orbital on the other. The greater delocalization of this level compared to 22a″ can be rationalized on the basis that the compressed axial geometry of the Mn^{III} ions destabilizes the majority spin d_{z^2} orbital on one metal center such that it lies reasonably close in energy to the minority spin d_{yz} orbital on the other.

III/IV Dimer. The structural parameters describing the optimized geometry of the mixed-valence dimer, $[Mn_2(\mu\text{-}O)(O_2CH)_2(NH_3)_6]^{3+}$, in Table 2 can be compared with the reported crystal structure of $[Mn_2(\mu\text{-}O)(OAc)_2(Me_3tacn)_2]^{3+}$ in Table 1. Due to the rigidity of the Me_3tacn ligand, the reported Mn−O and Mn−N distances exhibit very little difference between the two Mn centers. In contrast, the calculated structure of $[Mn_2(\mu\text{-}O)(O_2CH)_2(NH_3)_6]^{3+}$ exhibits distinct Mn^{IV} and Mn^{III} sites that can be easily distinguished on the basis of the Jahn−Teller distortion of the Mn^{III} ions. In particular, the $Mn^{IV}-O_c$ and $Mn^{III}-O_c$ distances differ by 0.18 Å, and similarly, the difference between $Mn^{IV}-N_{eq}$ and $Mn^{III}-N_{eq}$ is approximately 0.14 Å. Analogous to the III/III dimer, the longer $Mn^{III}-O_c$ and $Mn^{III}-N_{eq}$ bonds in the mixed-valence complex are consistent with the Mn^{III} center being high-spin and in a tetragonally compressed environment where the additional electron occupies the d_{xy} orbital. In the mixed-valence di-μ-oxo complex, $[Mn_2(\mu\text{-}O)_2(O_2CH)(NH_3)_6]^{3+}$, the Jahn−Teller distortion of the Mn^{III} site was shown to be noticeably smaller than that present in the III/III dimer due to the fact that the odd electron was partially delocalized over both Mn centers. In contrast, the Jahn−Teller distortion of the Mn^{III} site in $[Mn_2(\mu\text{-}O)(O_2CH)_2(NH_3)_6]^{3+}$ is comparable to that found in the calculated structure of the III/III dimer, indicative of a trapped valence system where the odd electron is effectively localized on the Mn^{III} site.

The presence of distinct Mn^{IV} and Mn^{III} sites in the mixed-valence dimer is consistent with the compositions of the molecular orbitals in Table 4b. The BS configuration corresponds to $(27a'\uparrow)^1(27a'\downarrow)^1(28a'\uparrow)^1(28a'\downarrow)^1(21a''\uparrow)^1(21a''\downarrow)^1(22a''\uparrow)^1$ with the odd electron occupying the 22a″↑ orbital. The fact that the metal contribution toward the 22a″↑ HOMO is composed almost entirely of the majority spin d_{xy} orbital on Mn^{III}, both confirms that the Mn^{III} center is high-spin and that the odd electron is localized. This analysis is also supported by the calculated net spin densities of +3.77 and −2.70 on the Mn^{III} and Mn^{IV} centers, respectively. Analogous to the IV/IV and III/III dimers, the magnetic coupling between the Mn centers occurs mainly via the symmetric $J_{xz/xz}$ and $J_{yz/yz}$ pathways, given the Mn_1:Mn_2 delocalization ratios of 35:16 and 43:11, respectively, for the 21a″↑ and 28a′↑ orbitals, with the most efficient pathway once again being $J_{xz/xz}$. The delocalization of the 27a′↑ orbital on the other hand, involving the symmetric $J_{x^2-y^2/x^2-y^2}$ pathway, is very small, similar to the III/III dimer. The almost complete localization of the odd electron occupying the majority spin 22a″ (d_{xy}) HOMO is in marked contrast with the rather high delocalization (36:24) of the equivalent but vacant orbital in the IV/IV dimer involving the crossed exchange $J_{xy/xz}$ pathway. The same localized scenario arose in the III/III dimer, and likewise in the III/IV dimer; this can be attributed to the Jahn−Teller stabilization of the majority spin d_{xy} orbital on Mn^{III} relative to the minority spin d_{xz} orbital on Mn^{IV}.

The HOMO−LUMO gap in Figure 6 is very small, with the 29a′↑ LUMO lying only 0.075 eV above 22a″↑. Attempts to optimize the geometry with different configurations resulted in higher energy structures in all cases. However, the optimized structure where the unpaired electron was forced into the minority spin 29a′ (d_{yz}) orbital, thus producing a low-spin Mn^{III} configuration, was found to be only 0.03 eV less stable than the BS high-spin configuration described above. The orbital compositions given in Table 4b for this alternative low-spin BS configuration paint a very different picture of electron delocalization, as the odd electron in the minority spin 29a′ orbital is found to be significantly delocalized (Mn^{IV}:Mn^{III} ratio of 29:45) via the crossed-exchange J_{yz/z^2} pathway. The large extent of delocalisation is also reflected in the calculated net spin densities of +3.35 and −2.31 on Mn^{IV} and Mn^{III}, respectively. The remaining occupied orbitals, 26a′, 28a′, and 21a″ are, however, similar in composition to those described above for the high-spin BS structure.

Comparison Between Oxidation States in $[Mn_2(\mu\text{-}O)(O_2CH)_2(NH_3)_6]^{n+}$. Overall the Mn−Mn separation decreases as the oxidation state is reduced from IV/IV to III/III but with only a small change of 0.03 Å in the first reduction step and a much larger change of 0.9 Å in the second. The changes in the Mn−Mn separation are accompanied by decreases in the Mn−O−Mn angle of 3° and 7°, respectively. Once again, the largest differences in the structures are associated with the Jahn−Teller distortion of the Mn^{III} centers. However, in contrast with $[Mn_2(\mu\text{-}O)_2(HCO_2)(NH_3)_6]^{n+}$, the Jahn−Teller axis is now orientated along the Mn−oxo bond rather than $Mn-O_c$, giving rise to axially compressed Mn^{III} geometries with long $Mn-O_c$ equatorial bonds. Thus, two-electron reduction of the IV/IV dimer causes a 0.15 Å increase in the $Mn-O_c$ distance and a 0.18 Å increase in the $Mn-N_{eq}$ distance. These structural changes stabilize the d_{xy} orbital relative to d_{z^2}, and therefore, the additional electrons occupy the former orbital on each Mn center in the III/III dimer. In the lowest energy structure for the mixed-valence dimer, the coordination environments about the Mn^{IV} and Mn^{III} centers closely resemble those in the IV/IV and III/III dimers, respectively, consistent with the mixed-valence complex being essentially localized. It is relevant to point out that complexes containing a $[Mn_2(\mu\text{-}O)(HCO_2)_2]^{n+}$ core with axially elongated Mn^{III} centers do exist, but in all cases these structures involve one or more terminal ligands which are not nitrogen donors.[20,61]

From earlier discussion, the magnetic coupling in the $[Mn_2(\mu\text{-}O)(HCO_2)_2(NH_3)_6]^{n+}$ system is largely determined by the relative efficiencies of the symmetric $J_{xz/xz}$ and $J_{yz/yz}$ antiferromagnetic exchange pathways and the ferromagnetic J_{yz/z^2} crossed exchange pathway. As can be seen from the schematics of these pathways shown in Figure 8, a change in the Mn−O−Mn angle does not affect the overlap of the d_{xz} orbitals on the Mn centers with the out-of-plane pπ orbital of the oxo bridge. Thus, the $J_{xz/xz}$ pathway is expected to be relatively insensitive to structural changes involving the Mn−O−Mn bridge. The effectiveness of the $J_{yz/yz}$ and J_{yz/z^2} pathways, on the other hand, depend very much on the Mn−O−Mn angle. As this angle becomes more acute, overlap of the Mn d_{yz} orbitals with the in-plane pπ orbital of the oxo bridge diminishes, and consequently, antiferromagnetic coupling via the $J_{yz/yz}$ pathway decreases. In contrast, overlap of the d_{yz} and d_{z^2} orbitals on opposite Mn centers with the in-plane pπ orbital of the oxo bridge is enhanced, and therefore, ferromagnetic coupling via this crossed exchange pathway increases as the Mn−O−Mn angle becomes smaller. These conclusions are reflected in the compositions of the 28a′ orbital. In the IV/IV dimer, the Mn_2 composition comprises mostly d_{yz} and a smaller amount of d_{z^2}, whereas in the III/III dimer, where the Mn−O−Mn angle is more acute, the d_{z^2} orbital contributes mostly to the Mn_2 composition. These conclusions also concur with those of earlier studies by Girerd and co-workers,[55] Weihe and Güdel,[56] and Corbella et al.[61]which demonstrated the importance of the crossed exchange J_{yz/z^2} pathway in the magnetic coupling of bent μ-oxo bridged dimers. Girerd and co-workers also showed that when the Mn−O−Mn angle is close to 120°, the $J_{yz/yz}$ pathway is negligible and the antiferromagnetic $J_{xz/xz}$ and ferromagnetic J_{yz/z^2} pathways become the dominant interactions. From extended Huckel studies, Corbella et al.[61] showed that ferromagnetic exchange was linked to axially compressed Mn^{III} centers whereas antiferromagnetic exchange was associated with axially elongated Mn^{III} coordination.

To gauge the importance of changes in the geometry of the Mn_2O core, the energies of the symmetric and antisymmetric combinations of the metal d orbitals in the S_{max} state for the III/III and IV/IV dimers are plotted as a function of the Mn−Mn separation in Figure 9. Unfortunately, extensive mixing between the metal and ligand orbitals, particularly for the IV/IV dimer, complicates the analysis. Furthermore, due to the delocalized nature of the S_{max} state, it is not possible to obtain information on the crossed-exchange J_{yz/z^2} pathway. However, the plots reveal that while the separation of the symmetric (+) and antisymmetric (−) combinations of d_{xz} orbitals is fairly constant with Mn−Mn distance, the separation of the d_{yz} orbital combinations is very sensitive to changes in this coordinate. From the separation of the (±) combinations of d_{xz} and d_{yz} orbitals, it can be concluded that the contributions of the $J_{xz/xz}$ and $J_{yz/yz}$ pathways are comparable in the IV/IV dimer, but in the III/III oxidation state there is a marked reduction in the contribution of $J_{yz/yz}$.

Consideration of the above geometrical arguments suggests that in the IV/IV dimer, which has the largest Mn−O−Mn angle of 133°, the ferromagnetic J_{yz/z^2} pathway will partially counteract the antiferromagnetic $J_{yz/yz}$, leaving the antiferromagnetic $J_{xz/xz}$ pathway to dominate the magnetic coupling. The IV/IV dimer

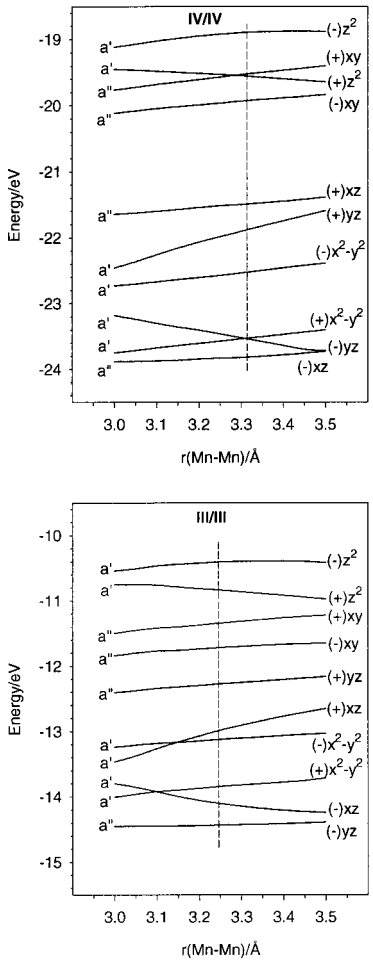

Figure 9. Energies of the symmetric (+) and antisymmetric (−) combinations of d orbitals in the high-spin state as a function of the Mn−Mn separation for (a) $[Mn_2(\mu\text{-}O)(HCO_2)_2(NH_3)_6]^{4+}$, (b) $[Mn_2(\mu\text{-}O)(HCO_2)_2(NH_3)_6]^{3+}$, and (c) $[Mn_2(\mu\text{-}O)(HCO_2)_2(NH_3)_6]^{2+}$. Vertical lines correspond to calculated Mn−Mn distances in BS state.

is therefore expected to exhibit the strongest antiferromagnetic exchange consistent with the significant delocalization of the 21a″ level in Table 4a. In the III/III dimer, the Mn−O−Mn angle is much closer to 120° where the $J_{yz/yz}$ pathway is negligible. Thus, the antiferromagnetic $J_{xz/xz}$ and ferromagnetic J_{yz/z^2} pathways are the principal interactions, in agreement with the delocalization and compositions of the 21a″ and 28a′ levels in Table 4a. To a large extent, the $J_{xz/xz}$ and J_{yz/z^2} pathways will cancel each other, and as a result, the magnetic coupling will be substantially weaker than in the IV/IV dimer. These arguments are in agreement with the calculated exchange constants of $-J = 180\ cm^{-1}$ and $-J = 25\ cm^{-1}$ (Table 5) for the IV/IV and III/III dimers, respectively, and highlight the importance of the crossed exchange J_{yz/z^2} pathway in the latter system, where the fortuitous cancellation of ferromagnetic and antiferromagnetic contributions leads to a relatively small overall exchange interaction. The same conclusions regarding the importance of the J_{yz/z^2} pathway in the III/III dimer were reached in the very recent study by Brunold et al.[62]

The mixed-valence III/IV dimer involving high-spin Mn^{III} has a Mn−O−Mn angle only slightly smaller than that of the IV/IV dimer. Therefore, we do not anticipate significant differences from that found in the IV/IV oxidation state,

(59) Delfs, C. D.; Stranger, R. Unpublished work.
(60) Schäfer, K.-O.; Bittl, R.; Zweygart, W.; Lendzian, F.; Haselhorst, G.; Weyhermüller, T.; Wieghardt, K.; Lubitz, W. *J. Am. Chem. Soc.* **1998**, *120*, 13104.
(61) Corbella, M.; Costa, R.; Ribas, J.; Fries, P. H.; Latour, J.-M.; Öhrström, L.; Solans, X.; Rodríguez, V. *Inorg. Chem.* **1996**, *35*, 1857.
(62) Brunold, T. C.; Gamelin, D. R.; Solomon, E. I. *J. Am. Chem. Soc.* **2000**, *122*, 8511.

particularly since the odd electron occupies the 22a″ level which corresponds to a highly localized majority spin d_{xy} orbital on Mn^{III}. By and large, these conclusions are supported by the compositions of the majority spin 28a′, 21a″, and 22a″ levels in Table 4b and the calculated exchange coupling constant of $-J = 154\ cm^{-1}$ in Table 5 for the III/IV dimer. In the alternative BS state where the Mn^{III} is low-spin, the odd electron occupying the minority spin 29a′ level is substantially delocalized (Mn^{IV}:Mn^{III} = 29:45) as a consequence of the crossed exchange J_{yz/z^2} pathway. Since this pathway is ferromagnetic, it will partially or even completely cancel the antiferromagnetic $J_{xz/xz}$ and $J_{yz/yz}$ interactions leading to relatively weak antiferromagnetic or ferromagnetic exchange in the ground state. The calculated ferromagnetic value of $J = 11\ cm^{-1}$ is consistent with this interpretation and is also in good agreement with the experimental values. Once again, the calculated value of $B = 401\ cm^{-1}$ will not reflect the dominant J_{yz/z^2} delocalization pathway, as the effect of this crossed exchange mechanism is eliminated due to the delocalized nature of the high-spin states used in eq 5. As a result of the significant delocalization via the crossed J_{yz/z^2} pathway in the alternative low-spin BS structure, the Mn^{IV} and low-spin Mn^{III} ions are partially converted to high-spin Mn^{III} and Mn^{IV}, respectively. Accordingly, two interacting spin ladders are associated with the low-spin BS structure, involving coupling of Mn^{IV} (S = 3/2) with low-spin (S = 1) and high-spin (S = 2) Mn^{III} centers. In addition to these spin-ladders is a third noninteracting spin-ladder arising from the localized high-spin BS structure described above. Since the low-spin and high-spin BS structures differ by only 0.03 eV, the Mn^{III} site clearly lies near the spin-crossover region, and therefore, all three spin-ladders in principle can contribute to the ground state. Thus, the calculations indicate that the ground state magnetic coupling in this complex is potentially quite complex.

Variation of the Bridging Ligand. Having discussed the variation in geometry and electronic structure of the $[Mn_2(\mu\text{-}O)_2(O_2CH)(NH_3)_6]^{n+}$ and $[Mn_2(\mu\text{-}O)(O_2CH)_2(NH_3)_6]^{n+}$ systems in each of the III/III III/IV and IV/IV oxidation states, we now turn our attention to the effect of the bridging ligands on the magnetic properties of these compounds. What is clear is that the electronic configuration of the metal centers, and thus the magnetic coupling in the dimer, is profoundly affected by changes to the bridging ligands. In particular, change in the bridging structure has a dramatic effect on the nature of the Jahn−Teller distortion observed for the Mn^{III} centers in the III/III and III/IV dimers. Our previous study of the tri-oxo $[Mn_2(\mu\text{-}O)_3(NH_3)_6]^{2+}$ dimer in the IV/IV oxidation state revealed that despite the very short Mn−Mn distance of 2.3 Å, the large antiferromagnetic coupling ($-J = 390\ cm^{-1}$) in this complex was mostly attributable to superexchange interactions involving the Mn d_{xz} and d_{yz} orbitals and the pπ orbitals of the bridging oxo ligands. As a result of the strong, covalent Mn-oxo bonds, the ligand field splitting of the majority spin t_{2g} and e_g orbitals is much larger than the spin-polarization splitting of the majority spin and minority spin t_{2g} orbitals on each Mn center, favoring low-spin Mn^{III} sites in both the III/III and III/IV dimers. This conclusion is in agreement with preliminary calculations on $[Mn_2(\mu\text{-}O)_3(NH_3)_6]$ and $[Mn_2(\mu\text{-}O)_3(NH_3)_6]^+$ which yield low-spin BS ground states.[59]

The removal of a single oxo bridge from the tri-μ-oxo complex to give the planar di-μ-oxo system $[Mn_2(\mu\text{-}O)_2(NH_3)_8]^{n+}$ increases the Mn−Mn separation by over 0.5 Å. High-spin Mn^{III} centers occur in both the III/III and III/IV dimers, and the Jahn−Teller effect gives rise to axially elongated Mn^{III} geometries with the distortion axis along the $Mn-N_{ax}$ bonds. The planar Mn_2O_2 core allows for efficient overlap of the Mn d_{xz} and d_{yz} orbitals with the out-of-plane oxo pπ orbitals, and so the magnetic coupling is dominated by the antiferromagnetic $J_{xz/xz}$ and $J_{yz/yz}$ pathways. Except for the mixed-valence dimer, the crossed exchange $J_{x^2-y^2/z^2}$ pathway makes only a minor contribution which maybe ferromagnetic or antiferromagnetic, depending on the occupancy of the $d_{x^2-y^2}$ and d_{z^2} orbitals. In the III/IV complex, the crossed $J_{x^2-y^2/z^2}$ pathway is responsible for partial delocalization of the odd electron.

Addition of a single carboxylate bridge to give the $[Mn_2(\mu\text{-}O)_2(O_2CH)(NH_3)_6]^{n+}$ system, results in the Mn_2O_2 core being tilted between 21 and 31°. In both the III/III and III/IV dimers, the Mn^{III} centers are high-spin, and the Jahn−Teller effect gives rise to axially elongated Mn^{III} geometries, with the Jahn−Teller axis along the $Mn-O_c$ bond. The most important effect of the tilt is that the overlap of both the d_{xz} and d_{yz} orbitals on Mn with the out-of-plane oxo pπ orbitals is diminished, and consequently, the symmetric $J_{xz/xz}$ and $J_{yz/yz}$ pathways are less efficient relative to the planar di-μ-oxo structure. In contrast, the crossed exchange $J_{x^2-y^2/z^2}$ pathway is more effective, leading to greater delocalization of the odd electron compared to the analogous planar di-μ-oxo system.

Replacement of one of the oxo bridges with a carboxylate ligand to give the $[Mn_2(\mu\text{-}O)(O_2CH)_2(NH_3)_6]^{n+}$ system causes significant structural change, in particular, the Mn−Mn separation and Mn−O−Mn angle both undergo dramatic increases of approximately 0.6 Å and 35°, respectively. Analogous to $[Mn_2(\mu\text{-}O)_2(O_2CH)(NH_3)_6]^{n+}$, the Mn^{III} centers are high-spin in the III/III dimer and also the lowest energy structure for the III/IV dimer. However, the Jahn−Teller axis is now orientated along the Mn−oxo bond giving rise to axially compressed Mn^{III} geometries with long $Mn-O_c$ equatorial bonds. For this bridging arrangement, overlap of the Mn d_{xz} orbitals with the out-of-plane oxo pπ orbital is unaffected by changes in the Mn−O−Mn angle, and therefore, the $J_{xz/xz}$ pathway is the dominant antiferromagnetic interaction. In contrast, the $J_{yz/yz}$ and ferromagnetic crossed J_{yz/z^2} pathways, involving overlap with the in-plane oxo pπ orbital, are very sensitive to the Mn−O−Mn angle. As this angle decreases, the $J_{yz/yz}$ pathway becomes less efficient while ferromagnetic coupling via the crossed J_{yz/z^2} pathway is enhanced leading to weak magnetic coupling in the reduced oxidation state. For the III/IV dimer, the BS structures involving low-spin and high-spin Mn^{III} are almost degenerate. In the high-spin case, the odd electron is essentially localized in the d_{xy} orbital on Mn^{III}, whereas in the low-spin alternative, significant delocalization occurs as a consequence of the crossed exchange J_{yz/z^2} pathway.

Acknowledgment. Financial support from the Australian Research Council (ARC) to R.S. is gratefully acknowledged.

IC0008767